RSP-413.8

Laboratory Triaxial and Permeability Tests on Tournemire Shale and Cobourg Limestone

(Contract 87055-14-0209: R413.8)

FINAL REPORT

M.H.B. Nasseri, Ph.D
and
R.P. Young, Ph.D

University of Toronto
Rock Fracture Dynamics Facility

February 2016

Table of Content:

Executive Summary

The aim of this experimental research investigation is to address tasks outlined by the Canadian Nuclear Safety Commission (CNSC) (Contract 87055-14-0209) to study coupled hydro-mechanical processes in sedimentary rocks such as limestone and shale with special attention to Excavation Damage Zone (EDZ) properties.

In this project a total of six hydro-mechanical experiments were performed on Cobourg limestone specimens prepared parallel and perpendicular to foliation planes. Three hydro-mechanical experiments were also performed on Tournemire shale (two tests on 0^o and one test on 45^o oriented specimens with respect to bedding plane). The first two specimens of Tournemire shale drilled at 0^o and 45^o orientation were tested following a short in situ saturation period and the third specimen (another 0^o sample) was tested after four hours of an in situ saturation procedure within the geophysical imaging cell.

The results show that Cobourg limestone specimens tested with their foliation planes parallel to the σ_1 direction are stronger (55%) than the specimens tested with their foliation planes perpendicular to the σ_1 direction. The graphical relationships showing the variation of permeability as a function of axial stress, for all of the six experiments on Cobourg limestone, indicate that the k values measured at post peak stresses are 2–3 orders of magnitude higher than the initial intact values irrespective of the foliation plane orientation.

The results from Tournemire shale show that specimens tested with the foliation plane oriented at 45^o with respect to σ_1 show a 12% strength reduction in comparison to specimens tested with their foliation planes oriented at 0^o with respect to σ_1. In comparison to Cobourg limestone, the variation between the measured maximum and minimum k values for Tournemire shale is one order of magnitude. Measurement of seismic wave velocities and their evolution with axial stress confirm the anisotropy in the specimens.

1 Introduction

This experimental investigation presents laboratory results of a collaborative project between the Canadian Nuclear Safety Commission (CNSC) and the Rock Fracture Dynamics Facility (RFDF) of the University of Toronto, initiated to study coupled hydro-mechanical (HM) effects on one sedimentary rock in Southern Ontario and the Tournemire shale obtained from France with special attention to excavation damage zone (EDZ) properties. Samples of the Cobourg limestone used in the experiments were collected based on a collaborative and joint site investigation between CNSC and RFDF. The block Cobourg limestone samples were collected at the St Marys quarry near Bowmanville, and the limestone specimens were cored (parallel and perpendicular to the foliation planes) at CANMET and delivered to the RFDF. Three specimens of the Tournemire shale were prepared at RFDF with the foliation planes oriented at 0^o and 45^o with respect to the σ_1 direction. The first two specimens of the Tournemire shale, drilled at 0^o and 45^o orientation, were tested following a 30 minutes of saturation period in the cell and the third specimen (another 0^o sample) was tested after four hours of saturation within the geophysical imaging cell based on the proposed testing procedure. A summary of the overall test results and their analyses relevant to the strength and transport properties of both rock types as a function of their foliation plane orientations are provided in this report.

The main objectives of this investigation is to understand the effect of oriented foliation planes on strength, deformation, transport, and seismic properties of the rock types tested at various differential stresses, the damage process of rocks, and post peak/post failure stress states with special references to the EDZ. Cobourg limestone is the candidate host rock for a proposed deep geological repository for the management of OPG's low and intermediate level radioactive wastes in Canada.

2 Experimental Methods

2.1 Physical property measurement

In this study, porosity was determined using the standard ISRM (1981a) water saturation porosity technique. First, the room temperature weight of all samples was measured. Then, the

samples were saturated with water under vacuum for more than a couple of months (to ensure full saturation), and the 100% saturated weights were taken. The dry and saturated densities of the specimen were then calculated. The difference between the dry and saturated weights of the samples was also used to calculate the effective porosity of the samples, using equation 1. Table 1 shows the experimental plan.

$$\Phi = \frac{V_r - V_{solid}}{V_r} = \frac{V_{pore}}{V_r} = \frac{Pore\ Volume}{Total\ Volume} \quad (1)$$

Where Φ is the porosity, V_r is the total volume, V_{solid} is the volume of solid within the rock, and V_{pore} is the pore volume. Table 2 shows the physical properties measured for Cobourg limestone based on aforementioned approach.

2.2 Permeability measurement

50.5 mm diameter specimens with an approximate length of 125mm were tested for permeability evaluation within a geophysical Hoek type imaging cell during triaxial compressive strength determination for the HM experiments. Permeability of the Cobourg limestone and Tournemire shale were measured as a function of hydrostatic stress of 5 MPa at a room temperature of about 25°C and various axial loading pressures. A transient method (pulse decay method) suggested by Brace et al. (1968) was used for the experiment and calculation of permeability. This method involves a small-step change of pore pressure imposed at one end of the sample after the specimens were exposed to 3 MPa of pore water pressure from both ends while maintaining 5 MPa of hydrostatic stress. Then pore pressure decay at one end of the sample is then measured by introduction of additional 1 MPa of hydraulic pulse. The pressure gradient decays exponentially to zero, and the pressure P_1 in reservoir 1 (Figure 1, Appendix A) is given by equation 2.

$$(P_1 - P_f) = \Delta P \left[V_2 / V_1) + V_2\right] e^{-\alpha t} \quad (2)$$

Where A is the cross-sectional area, L is the length of sample, V_1 and V_2 are volumes of reservoirs 1 and 2 (Figure 1, Appendix A), P_f is the final pressure, μ is viscosity of the water, β is conversion constant and ΔP is the step change of pressure in reservoir at time = 0. The

permeability k of the sample is found by plotting the pressure decay (P_1 - P_f) on a semi-log scale over time, t. The slope of the resulting line is $-\alpha$, while permeability is derived from equation 3.

$$\alpha = (kA/\mu\beta L)\,(1/V_1 + 1/V_2) \qquad 3$$

The next step involved increasing the differential stress at a constant rate.

Table 1. Experimental plan

Experiments	No. of test required	Time for test	Time analysis & report	Remarks
Sample preparation (coring, cutting, lapping)	Minimum of 6 for Cobourg limestone and 3 for Tournemire shale	One month	-	Sample preparation for Tournemire shale
Physical property measurement (porosity, dry/saturated density)	Nine specimens of Cobourg limestone Six was tested under triaxial stress	Four months for full saturation (Samples were weighed till no more water adsorption was recorded)	Two months	No Tournemire specimen for perpendicular to the foliation plane was made
HM experiments in triaxial geophysical imaging cell (GIC)	9 tests, i.e. three specimen parallel to the bedding plane and three normal to it for Cobourg and three tests parallel and 45 ^{o} to bedding planes for Tournemire shale. Test were conducted under drained condition	One year	Four months	TS0-1 was tested under a quick saturation period. TS0-2 was tested under 4 hours saturation period, B values at three levels were calculated for TS0-2
Final report	Analysis of the all data		Feb., 2016	

(Specimens: L=125 mm and D=50 mm.)

Table 2. Physical properties of Cobourg limestone measured at RFDF.

Specimens	**L** cm	**Diameter** cm	**Dry weight** g	**Saturated weight** g	**Porosity** %	**Dry Density** g/cc	**Saturated Density** g/cc
CLV-1-T	12.50	5.40	666.26	668.61	0.82	2.33	2.34
CLV-3-T	12.50	5.40	659.58	663.17	1.26	2.31	2.32
CLV-4-U	12.50	5.40	663.26	665.63	0.83	2.32	2.33
				Average	**0.97**	**2.32**	**2.33**
				Standard Deviation	**0.25**	**0.01**	**0.01**
CLH-1-T	12.50	5.40	666.48	668.90	0.85	2.33	2.34
CLH-1-U	12.50	5.40	667.59	669.70	0.74	2.33	2.34
CLH-2-T	12.50	5.40	666.62	669.34	0.95	2.33	2.34
CLH-2-U	12.50	5.40	664.64	667.20	0.90	2.32	2.33
CLH-3-T	12.50	5.40	664.18	666.83	0.93	2.32	2.33
CLH-3-U	12.50	5.40	663.67	666.77	1.09	2.32	2.33
				Average	**0.91**	**2.33**	**2.34**
				Standard Deviation	**0.12**	**0.01**	**0.00**

CLV= Specimens prepared perpendicular to foliation plane, CLH= Specimens prepared parallel to foliation planes.

Once the target differential stresses were achieved the pulse decay method was applied to measure the new permeability value (k) at that stress level using same 1 MPa of hydraulic pulse. After failure of the specimen, the permeability was measured again. Based on our experimental procedure, the deferential stress was raised at a strain rate of 1.6×10^{-6} until failure and beyond failure regimes. The servo-controlled load was kept on hold during measurement of a new k (m^2) value. Prior to all permeability measurements using pulse decay method, the testing cell's upstream and downstream storage factor have been evaluated using a steel sample of same size as that of rock specimens following methods outlined by Boulin et al. 2012.

2.3 Hydro-mechanical experiments under hydrostatic and differential stresses using a geophysical imaging cell (GIC)

In total nine samples of 50.5 mm diameter and 125 mm length were tested under hydrostatic and differential stresses with a confining pressure of 5 MPa and a pore pressure of 2 MPa. The testing parameters were discussed between RFDF and CNSC experts to evaluate the HM properties of the excavation damage zone which is a prime task of this investigation. The geophysical imaging cell (Figure 1) is equipped with ultrasonic-wave velocity stacks oriented

along three orthogonal axes of X, Y and Z, enabling us to measure the evolution of compressional and shear wave velocities as a function of deferential stresses. During an experiment the saturated samples (except for Tournemire shale specimens) were first gradually loaded to a 5 MPa hydrostatic pressure, after which the pore water pressure was raised to 3 MPa. The MTS axial actuator was held under constant displacement control mode once the axial stress reached around 5 MPa. Simultaneously the confining pressure was raised to 5 MPa using a servo-control Teledyne system. Attempts were made to carry out seismic wave velocity measurements at equal stress intervals prior to failure and at hydrostatic stress. This was done in conjunction with measuring the permeability of the specimen at ambient temperature using the pulse decay method at 5 MPa of hydrostatic stress and at various differential stresses. A servo-control Quizix pump (two pump systems) under independent constant control mode was used to regulate the top and bottom pore pressures and to generate hydraulic pulses for measuring k under a hold position for axial load conditions at targeted axial stresses up to the post failure region. These tests were conducted under a drained condition.

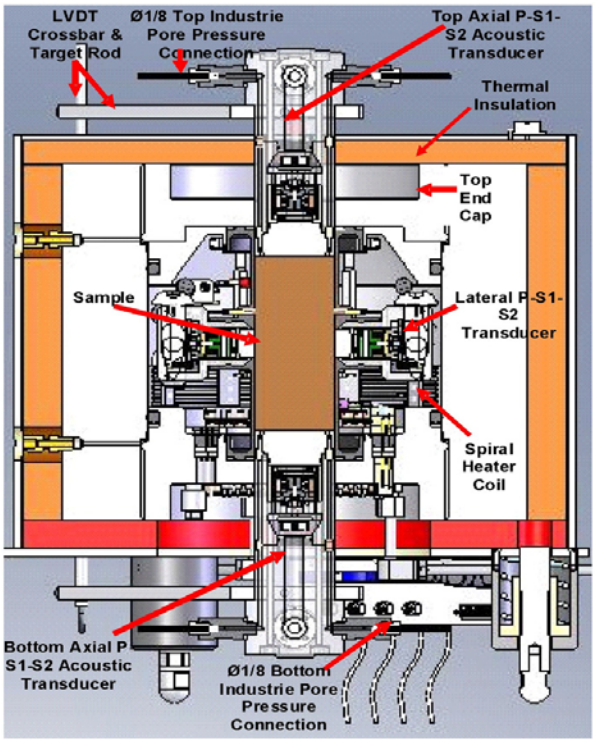

Figure 1. The geophysical imaging cell's internal view of the confining rubber and the X and Y and Z direction velocity stacks along with rock specimen.

During the experiments, in addition to the MTS axial deformational measuring unit, two separate LVDTs were used to measure axial deformation of the specimen (integrated part of GIC) close to the specimen outside the cell. The diametral strain of the specimen as a function of the axial stress was determined using an inbuilt cantilever system within geophysical imaging cell.

3 Experimental Results and Discussion

The experimental results are divided into two parts. First is the determination of physical properties of Cobourg limestone. The second part shows the variation and coupled evolution of ultrasonic-wave velocities, and transport properties as a function of hydrostatic and deferential stresses and is used for overall interpretation of coupled HM processes in the context of EDZ.

3.1 Physical properties

Determination of the physical properties of Cobourg limestone have been carried out based on ISRM specifications; the results are presented in Table 2. These specimens showed porosity values varying from 0.74% to 1.26%, which is considered extremely low for porous carbonate rocks. Since Cobourg limestone can be considered as a rock with extremely low porosity, saturated and dry densities do not differ a lot from each other, and vary between 2.3 g/cc and 2.4 g/cc. The physical properties for Tournemire shale is not reported here because water could not be used to evaluate their porosity and densities the way that was done for Cobourg limestone. Coring of Tournemire shale specimens into smaller diameter was possible using air pressure as cooling fluid under vacuum.

3.2 Triaxial compressive strength of Cobourg limestone under HM experiment

Cobourg limestone specimens CLH-3-T, CLH-1-U, and CLH-3-U prepared with foliation planes parallel to the long axis of the specimens and specimens CLV-3-T CLV-1-U and CLV-5-T prepared with foliation planes perpendicular to the long axis were tested at a 5 MPa confining pressure within the geophysical imaging cell according to the experimental method and testing procedure explained in section 2.3. The results for the specimens with foliation planes oriented parallel and perpendicular to the long axis of the specimen are included here.

3.2.1 Specimen CLH-3-T (parallel to foliation plane)

Figure 2 shows the variation of axial, diametral strains, and permeability values at differential stresses up to failure and into the post-failure regime for specimen CLH-3-T. Specimen CLH-3-T failed at an axial stress of 90 MPa, experiencing 0.45% and 0.54% of axial and diametral strain respectively. Figure 3 shows the failure pattern of the specimen after the test.

The permeability at around 10 MPa differential stress was measured to be around 2.3E-19 m^2 and the variation of the permeability is shown as a function of axial strain in the secondary vertical axis in Figure 2. The k value for CLH-3-T decreased to 1.4E-19 and then increased to 3.7E-19 m^2 as the axial stresses were raised up to 35 and 65 MPa respectively reflecting the initial compaction followed by initiation of fracturing. Further increment of k (8.9E-19) measured at σ_1 = 85 MPa could be related to the creation of more micro-fractures formed at the onset of plastic deformation of the specimen happening beyond 60MPa of axial stress (based on declining lateral compressional seismic velocities values).

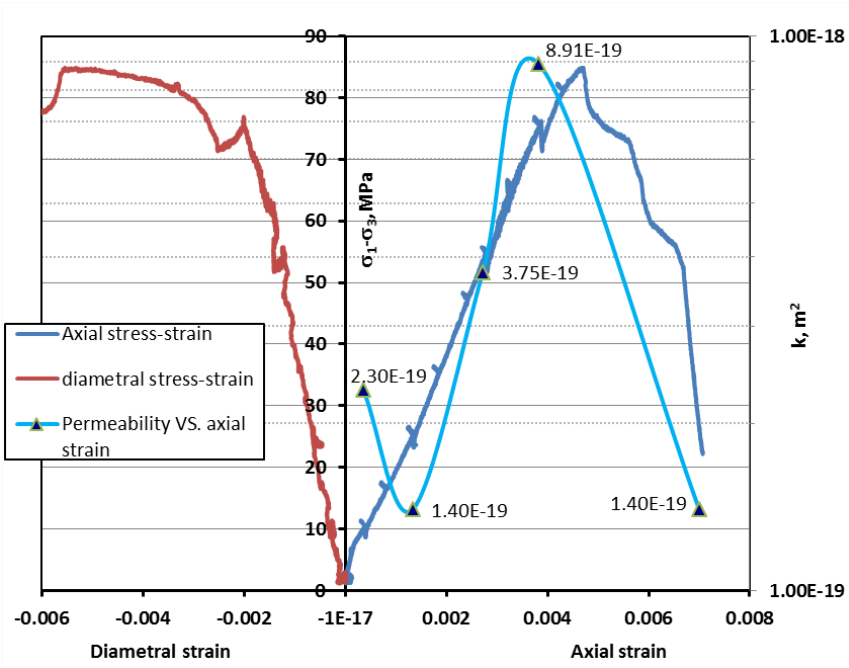

Figure 2. Variation of axial (average of two axial LVDT) and diametral strains with differential stresses for specimen CLH-3-T tested at a 5 MPa confining pressure and 3 MPa pore pressure, respectively. Variation of k is shown in the figure with respect to axial strain. The hydraulic pulse was introduced from the top end of the specimen.

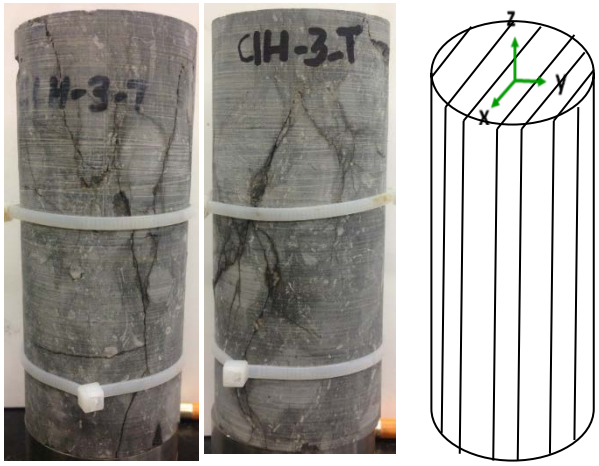

Figure 3. Failure pattern observed for the specimen CLH-3-T shown at two different angles. The sketch shows the 3D orientation of wave velocity measurements with respect to the foliation planes.

The k value measured, almost near post peak stress, shows a value double that of the previous k measured at the 60 MPa axial stress. The post failure k was found to be 1.4E-19 m^2. In this experiment, we did not observe an increased k value for a post failure stress. This anomaly could be due to couple of factors such as interaction of failure planes in the specimen with the top loading platen within the cell and the spatial coincidence between the water distribution ring in the platen from where the hydraulic pulse is sent and the failed surfaces in the specimen. It should be emphasized here that during the pulse decay process within the cell, creating a hydraulic pulse that can affect the other end of the specimen is almost impossible due to the length of the specimen, the shorter time for monitoring the hydraulic decay, and the impermeable nature of the rock tested. The decay of a hydraulic pulse with time can be measured within a short length of the specimen from the pulsing end of the specimen and the induced changes that happen within that region as a function of differential stress increments. These values of k and their evolution as a function of axial stresses are in good agreement with the earlier investigation RFDF carried out in a collaborative research investigation on THM properties of Cobourg limestone (Nasseri et al., 2013).

3.2.1.1 Evolution of ultrasonic wave velocities with differential stress increment

This section reports the results regarding the evolution of seismic wave velocities (compressional and two shear wave velocities) as a function of differential stress increments up to failure and beyond for the CLH-3-T. Figures 4-7 show the compressional (V_P), shear (Vs_1 and Vs_2) seismic wave velocities and shear wave splitting (SWS). Shear wave splitting is the phenomenon that occurs when a polarized shear wave enters an anisotropic medium and is typically used as a tool for measuring the degree of anisotropy of an area of interest and is calculated in percent; [(V_{S1}-V_{S2})/V_{S1} x 100]. V_P continuously increases along the Z direction, which is parallel to the σ_1 loading direction up to a differential stress of 80 MPa. The specimen was placed within the cell with its foliation planes parallel to the X axis velocity sensor. V_{PX} show a higher value of velocity profile than V_{PY} due to preferable alignment of foliation planes along XZ plane (Figure 3 and Figure 4). V_P measured along two horizontal directions (X and Y) initially showed a little increase up to a differential stress of 50 MPa, followed by a total decrease of about 0.15 km/s as deferential stress increased to 80 MPa. V_P for the Y direction experienced a decrease starting at 50 MPa because the Y axis velocity sensor measures the evolution of compressional wave velocity perpendicular to the foliation planes (Figure 4). Figures 5 and 6 show shear wave velocity V_{S1} and its polarization (V_{S2}) as a function of axial stress along three perpendicular directions (X, Y and Z axes) for the CHL-3-T, respectively. Along the σ_1 loading direction (Z axis), V_{S1Z}, and V_{S1X} show higher velocities than V_{S1Y}, since the foliation planes are oriented perpendicular to Y axis and wave propagation direction coincides with the preferably oriented foliation planes running along XZ plane. V_{S1Z} show an increasing trend due to the fact that induced vertical fracture cannot be detected by the axial (Z) sensor.

Figure 7 shows the shear wave splitting (SWS) and its variation measured along three directions as a function of axial stress increments. The percentages of SWS along X and Z axes are higher than the Y axis, which reflects on the anisotropic nature of specimen and thus the effect of vertically oriented weak planes (parallel to XZ plane) on shear velocity changes. Progressive compaction of the specimen reduces the SWS along both axes, i.e. 10% and 3% for Z and X axes, respectively, prior to failure.

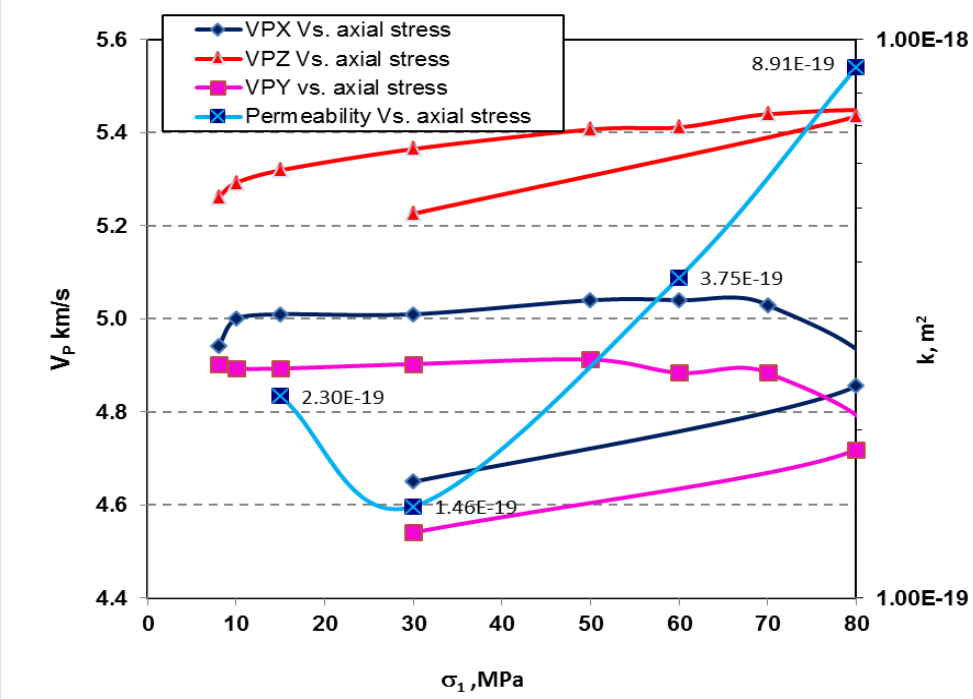

Figure 4. Variation of compressional wave velocities measured along three orthogonal axes and permeability values with axial stress for CLH-3-T specimen.

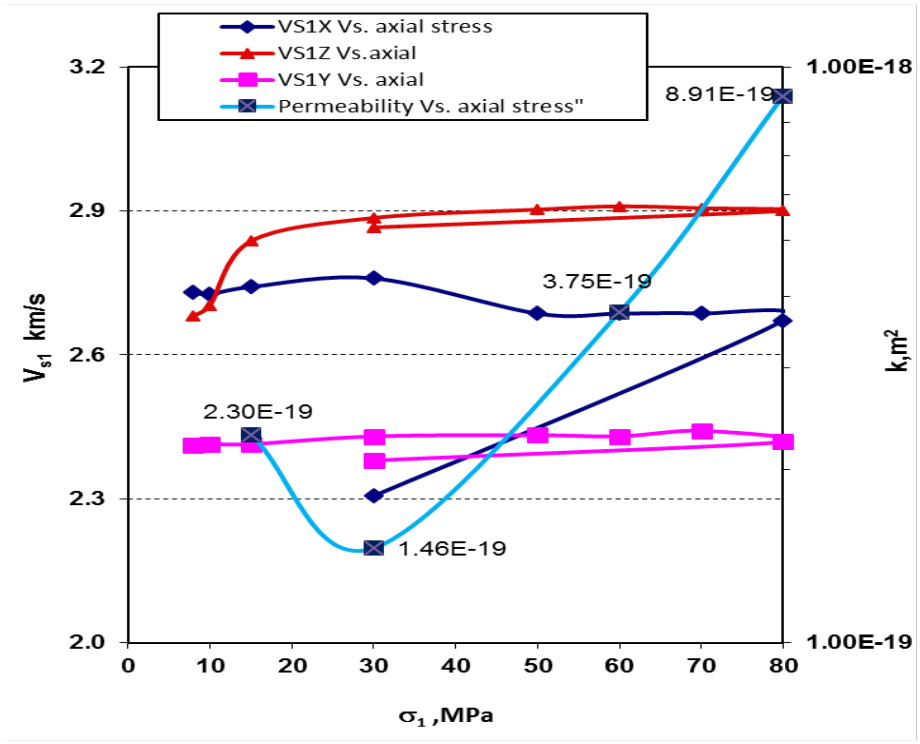

Figure 5. Variation of shear wave velocity V_{S1} and permeability values as a function of axial stress.

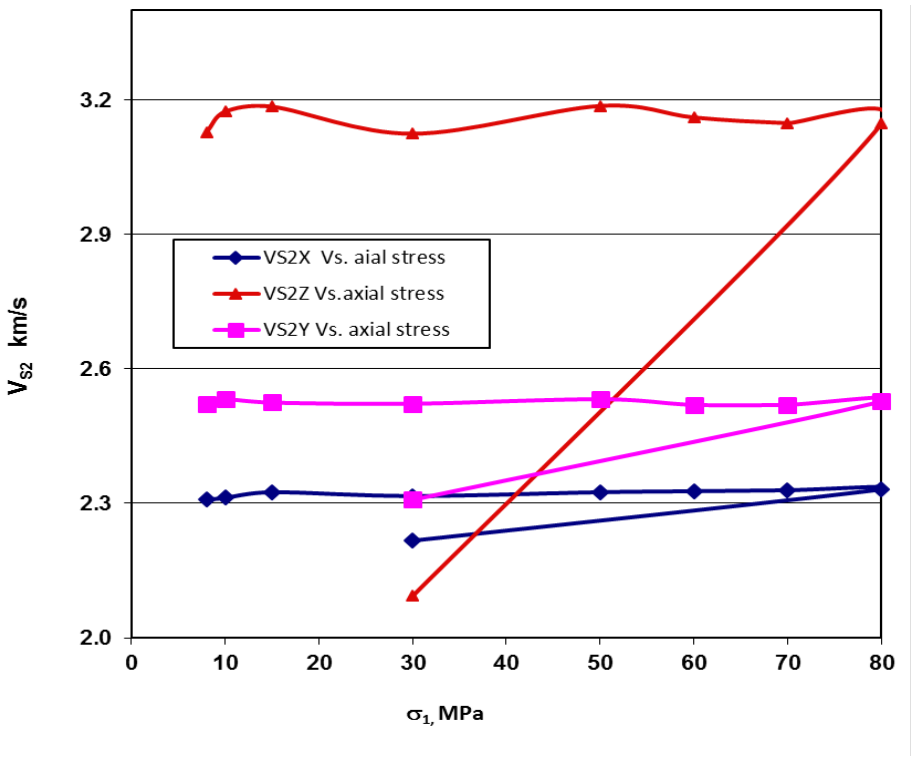

Figure 6. Variation of shear wave velocity, V_{S2} and permeability values as a function of axial stress.

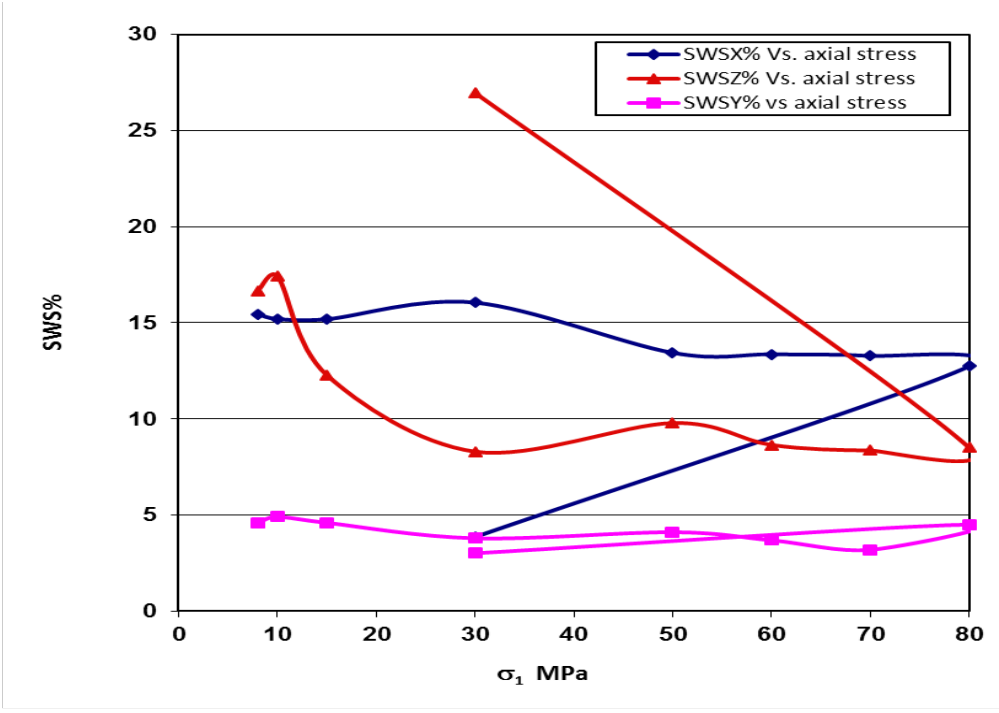

Figure 7. Variation of SWS% as a function of axial stress for CLH-3-T.

3.2.2 Specimen CLH-1-U (parallel to foliation plane)

Figure 8 shows the variation of axial, diametral strains at various differential stresses up to failure and beyond failure regimes for specimen CLH-1-U tested under similar testing procedure used in the first experiment. Permeability as a function of axial strain is shown in the same graph in the second vertical axis.

This specimen failed at 99 MPa of differential stress with a maximum axial strain of 0.45% and a diametral strain of 0.18%. The overall trend of permeability measurements for this specimen follows similar path as that of specimen CLH-3-T with the exception that the current specimen's post failure k shows almost four orders of magnitude higher than the permeability measured at 20 MPa of axial stress. With this observation we can interpret that at least some of the failure surfaces made under the axial loading platen were exposed to the hydraulic pulses during post failure measurement of permeability unlike the situation described for specimen CLH-3-T. The initial k value of 1.46E-19 measured at 20 MPa of differential stress was found to be reducing to a value of 9.78E-20 when the differential stress was increased to 40 MPa. This implies that the compaction effect caused closure of the pores and micro-fractures to communicate with each other at a lower axial stress. This situation has changed with further increments of differential stress to 65 and 85 MPa where the k value increased to 4.39E-19 and 8.15E-18 m^2. The latter measurement of k value corresponds to a stress regime of pre-peak domain in which formation of numerous axial micro-cracks makes the specimens more permeable beyond its linear section of stress-strain curve. The post failure k shows the fractured Cobourg limestone specimen tested parallel to the foliation planes may indicate the transport properties of EDZ under 5 MPa of confining pressure with 3 MPa of pore pressure applied to the failed region (i.e. effective confining pressure of 2 MPa). The severity of the post failure damage (Figure 9) and its comparison with the intact situation are further manifested by the seismic wave velocity changes in the tested specimens and will be discussed in the next section. Figure 9 shows the comparison of the intact specimen with that tested and a sketch of the specimen with its foliation plane orientation with respect to 3D direction of wave velocity measurements.

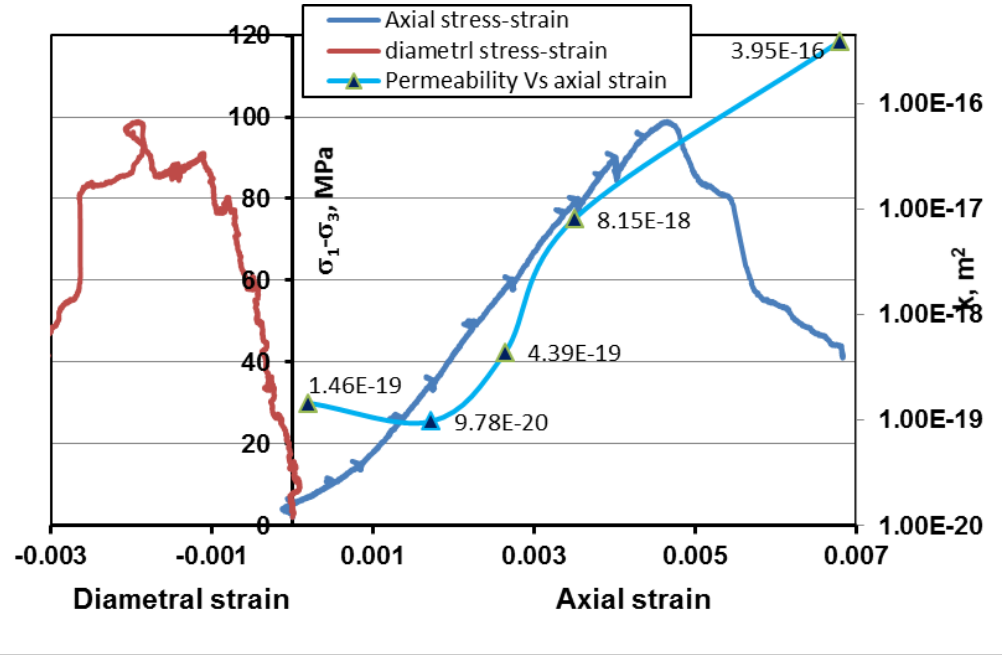

Figure 8. Variation of axial and diametral strains with differential stresses for specimen CLH-1-U tested at 5 MPa and 3 MPa of confining and pore pressures respectively. k as a function of axial strain is shown in the second vertical axis. The hydraulic pulse was introduced from the top end of the specimen.

Figure 9. Comparison of failure pattern (middle images taken at two different angles) observed for the tested specimen CLH-1-U with that of intact one (image on the left). The sketch shows the 3D orientation of wave velocity measurements with respect to the foliation planes.

3.2.2.1 Evolution of seismic wave velocities with differential stress increment

Figures 10 to 14 show the variation of the compressional (V_P), shear (Vs_1 and Vs_2) seismic wave velocities and shear wave splitting (SWS) as a function of axial stress for specimen CLH-1-U. A similar trend is observed for the earlier specimen showing the reproducibility of seismic properties in the specimens tested parallel to the foliation planes. V_P continuously increases along the Z direction, which is parallel to the σ_1 loading direction up to a differential stress of 100 MPa.

V_{PZ} and V_{PX} show a higher profile than V_{PY} (Figure 10) due to the coincidence of XZ plane with X and Z axes compressional wave velocity propagation directions. The effect of anisotropic planes oriented parallel to the XZ plane in the specimen is well documented in the behaviour of two horizontal shear wave velocities oriented at polarized directions. V_{S1X} and V_{S1Z} measured parallel to X and Z axis with their planes of propagation parallel to the XZ plane show a higher velocity profiles than that of V_{S1Y} which is forced to propagate normal to the foliation plane (Figure 11).

Figure 13 shows SWS% as a function of axial stress, measuring the anisotropic nature of Cobourg limestone being tested with their foliation planes parallel to the axial stress direction. SWS for X and Z axes shows a higher degree of anisotropy due to presense of XZ plane than that of XY plane.

3.2.3 Specimen CLH-3-U (parallel to foliation plane)

Figure 14 shows the variation of axial, diametral strains at differential stresses up to failure and beyond failure regimes for specimen CLH-3-U. Variation of k as function of axial strain is also shown in the figure. This specimen failed at 77 MPa of axial stress with a maximum axial strain of 0.46% and a diametral strain of 0.06%. The overall trend of permeability measurements for this specimen follows similar path as that of previous specimens with the exception that the current specimen showed a progressive decreasing trend of k value as a function of axial stress

up to 60 MPa of differential stress. The post failure k value shows a remarkable increase in k value of 1.50E-18 changing from 1.9E-19 measured at 60 MPa of differential stress.

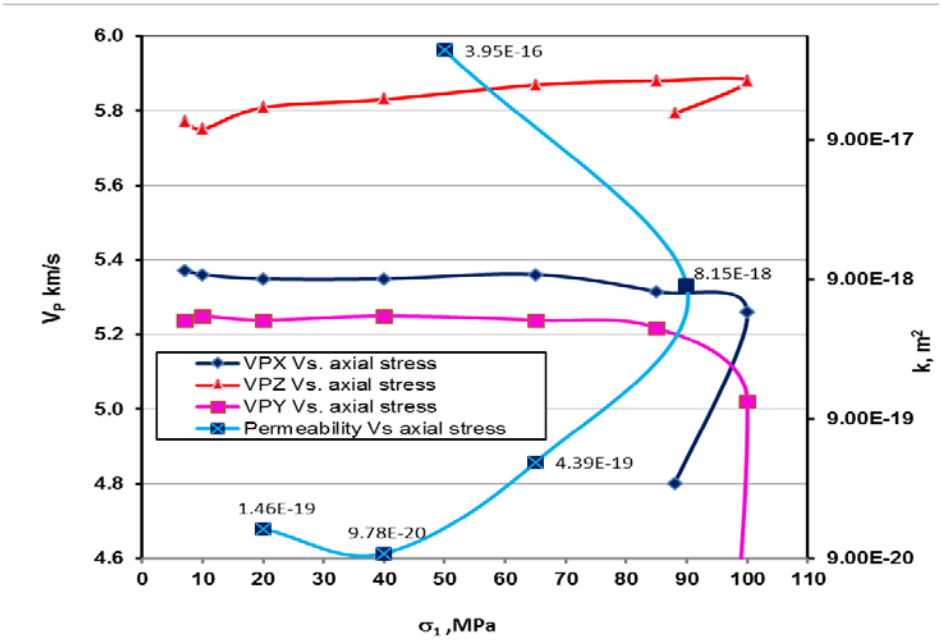

Figure 10. Variation of compressional wave velocities measured along three orthogonal axes and permeability values with axial stress for CLH-1-U specimen.

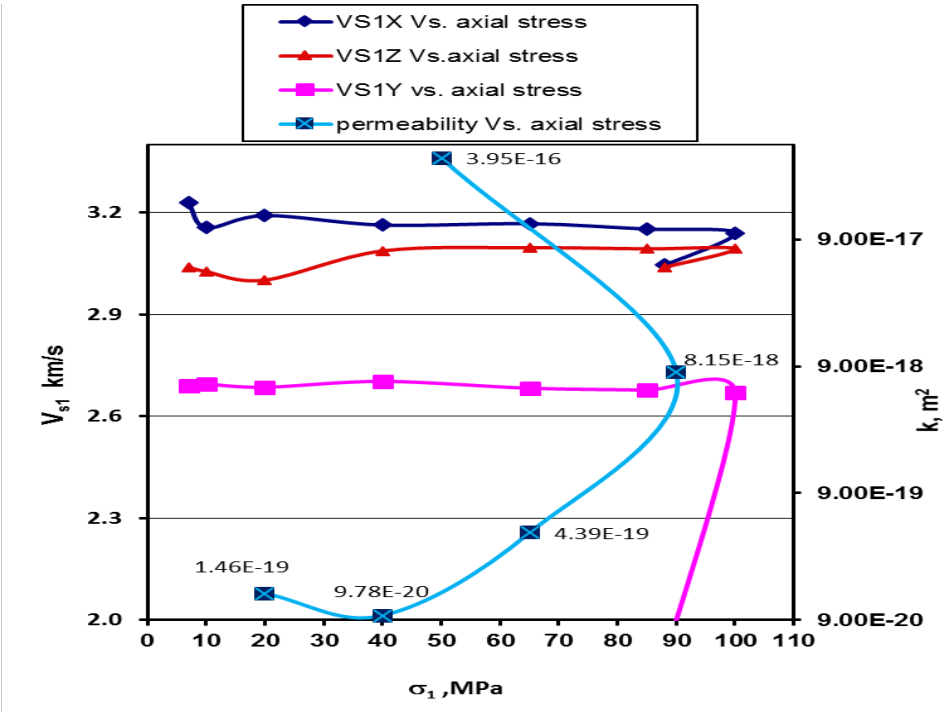

Figure 11. Variation of shear wave velocity, V_{S1} and permeability as a function of axial stress.

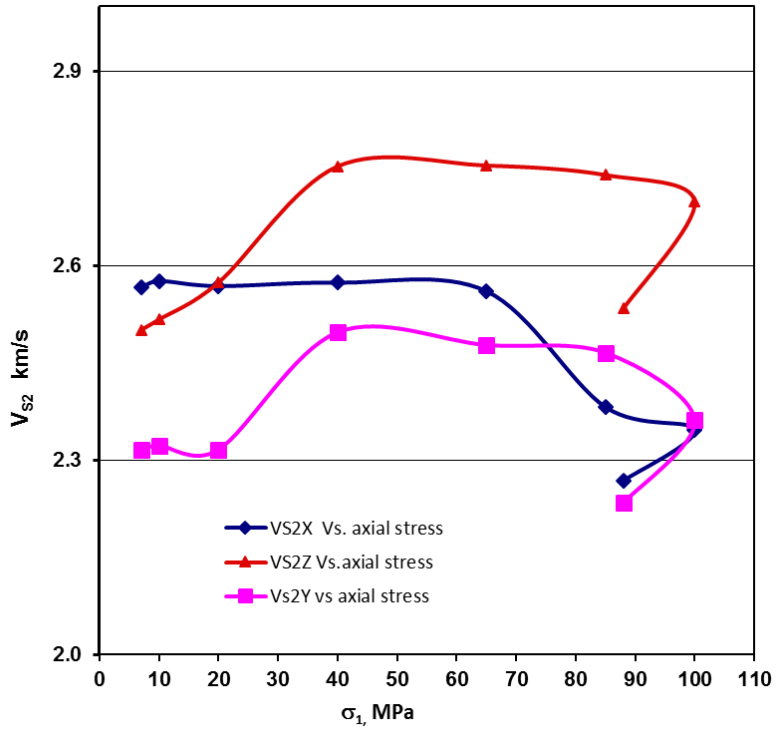

Figure 12. Variation of shear wave velocity, V_{S2} and permeability values as a function of axial stress.

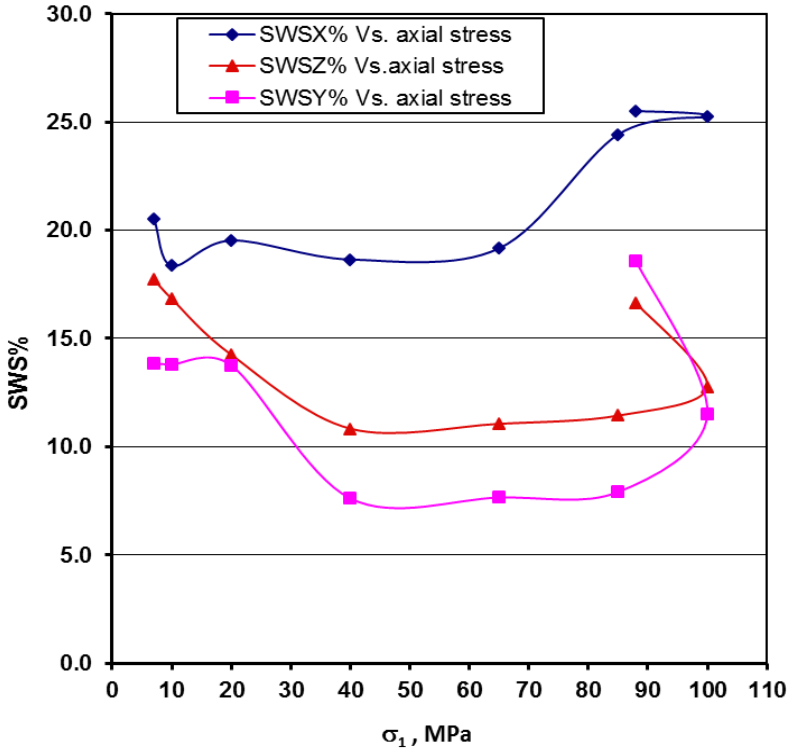

Figure 13. Variation of SWS% as a function of axial stress for CLH-3-T.

This experiment is another proof of the situation where some failed surfaces made under the axial loading platen were exposed to the hydraulic pulses during post failure measurement of permeability similar to what has happened in CLH-1-U. The initial k value of 4.88E-19 measured at a differential stress of 6 MPa was found to be reduced to a value of 3.28E-19 when the differential stress was increased to 10 MPa followed by continuous decline in permeability as differential stress was raised up to 60 MPa reaching to 1.9E-19. This implies that the compaction effect causing the closure of the pores and micro-fractures are communicating with each other at a lower axial stress in this specimen was not as severe as CLH-1-U. The post failure k, specimen CLH-3-U measured at a residual stress of 27 MPa seems to be two order of magnitude lower than that of post failure for CLH-1-U measured at a residual stress of 55 MPa. Data obtained from the last two experiments show that the transport property (i.e. k = 3.9E-16 m^2) of a highly damaged EDZ in Cobourg limestone can change in four orders of magnitude in comparison with same specimen at a fully compacted state (i.e. k = 9.7E-20 m^2 measured prior to any damages). Figure 15 shows the intact and tested photos for specimen CLH-3-U. A sketch in the same figure shows the alignment of foliation plane with 3D direction of seismic wave velocity measurements. Figures 16 to 19 show all the seismic velocity variation of tested specimen as a function of axial stress in the same manner discussed for earlier specimens. The overall similarity of the said properties and its variation confirms the reproducibility of these properties and the influence of inherent anisotropy seen within Cobourg limestone specimens prepared to the foliation planes.

3.2.4 Specimen CLV-3-T (perpendicular to foliation plane)

Figure 20 shows the variation of axial, diametral strains and permeability values at differential stresses up to failure and beyond failure regimes for specimen CLV-3-T tested at 5 MPa of confining pressure and 3 MPa of pore water pressure induced from both ends of the specimen. This specimen failed at 45 MPa of differential stress with a maximum axial strain of 0.3% and a diametral strain of 0.3%. The triaxial compressional strength of the specimens tested perpendicular to foliation plane is lower than the ones tested parallel to foliation plane. The overall trend of permeability measurements for this specimen follows similar path to that of previous specimens tested parallel to foliation planes.

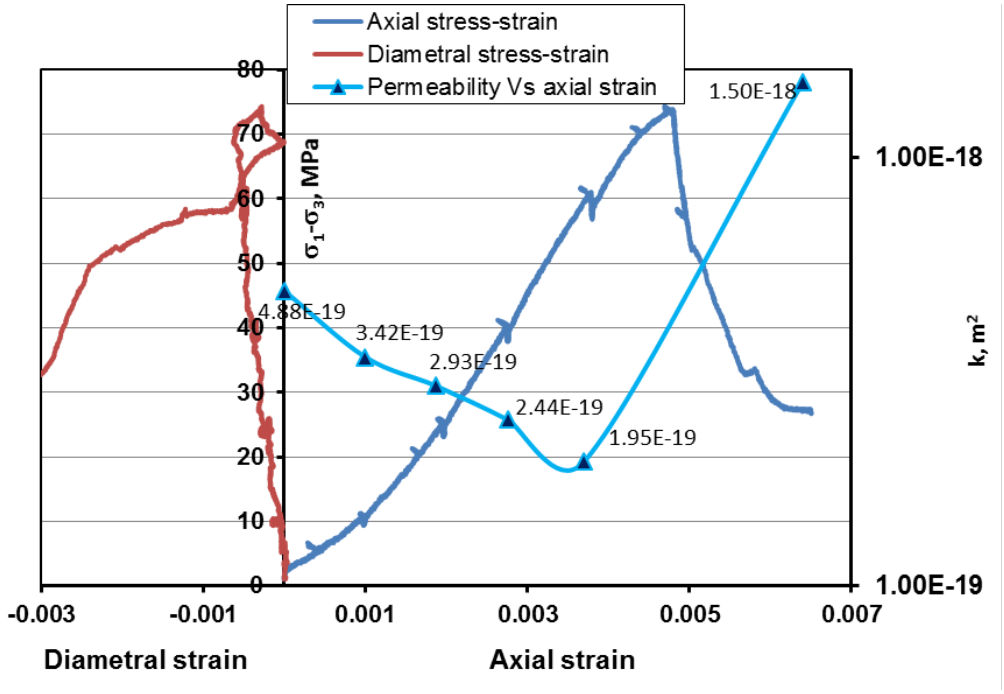

Figure 14. Variation of axial and diametral strains with differential stresses for specimen CLH-3-U tested at 5 MPa and 3 MPa of confining and pore pressures, respectively. Variation of permeability as a function of axial strain is shown in the second vertical axis. The hydraulic pulse was introduced from the top end of the specimen.

Figure 15. Comparison of failure pattern (two images in the middle) observed for the tested specimen CLH-3-U with that of intact one (image on the left). The sketch shows the 3D orientation of wave velocity measurements with respect to the foliation planes. The hydraulic pulse was introduced from top of the specimen.

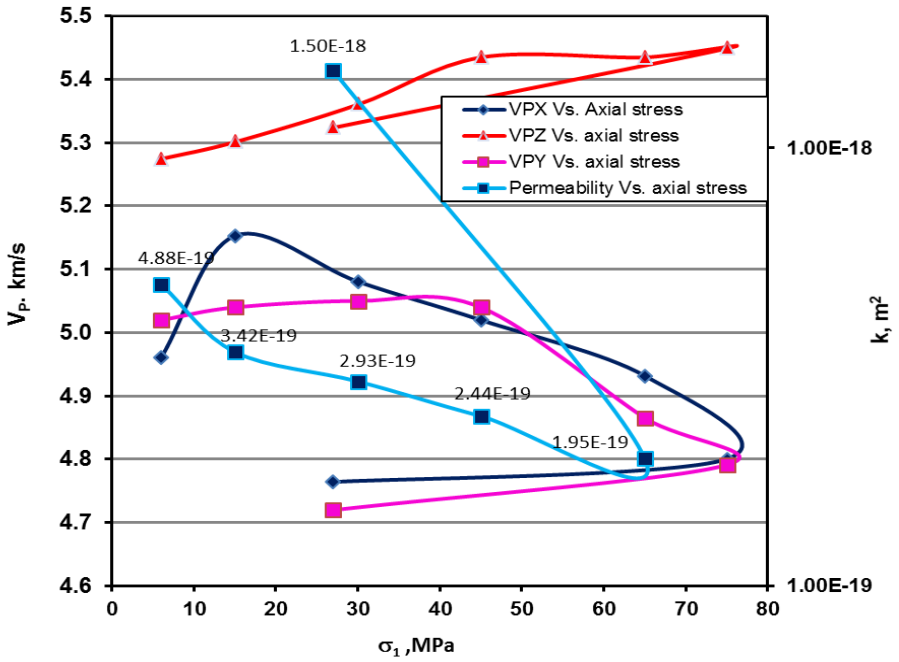

Figure 16. Variation of compressional wave velocities measured along three orthogonal axes and permeability values with axial stress for CLH-3-U specimen.

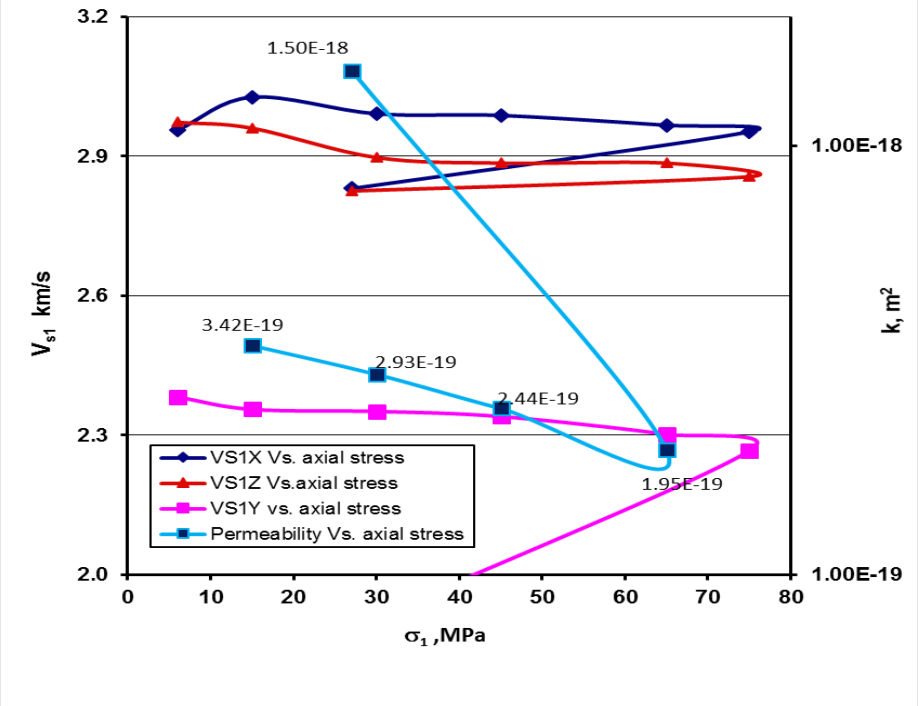

Figure 17. Variation of shear wave velocity V_{S1} and permeability as a function of axial stress.

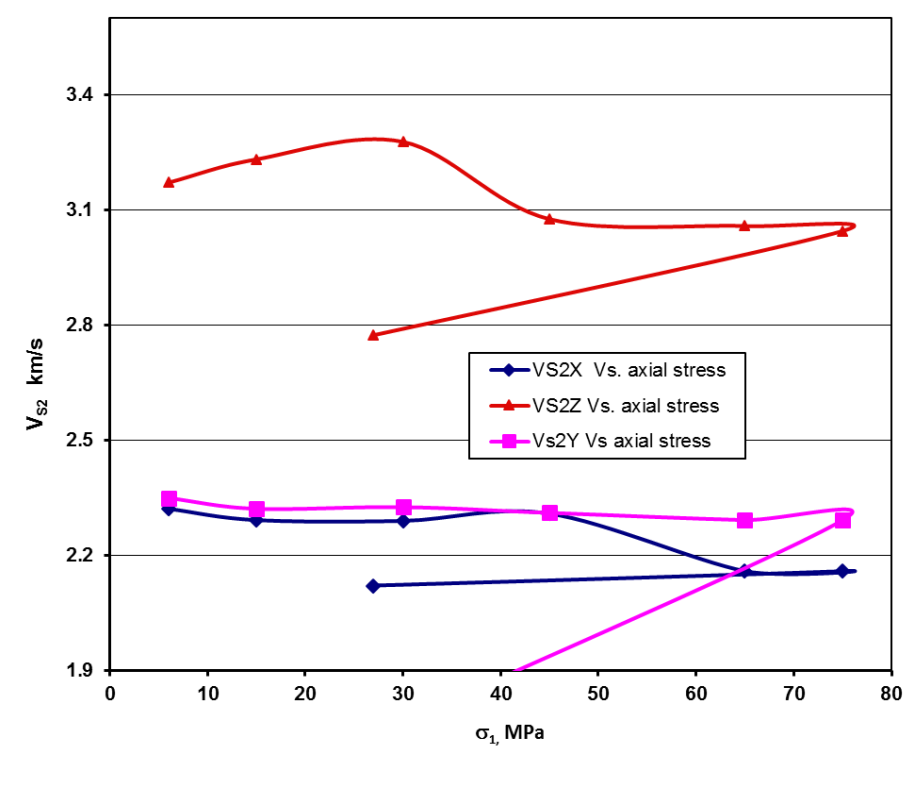

Figure 18. Variation of shear wave velocity V_{S2} as a function of axial stress.

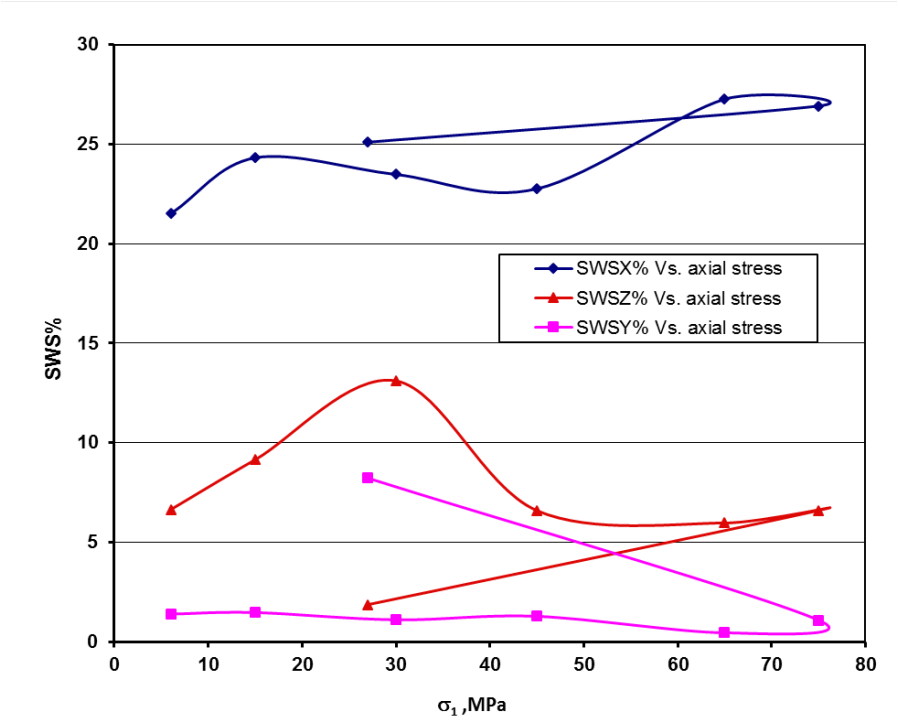

Figure 19. Variation of shear wave splitting, SWS% as a function of axial stress.

The current specimen shows a progressive increasing trend of k value as a function of axial stress up to post failure stress. The post failure k value for this specimen shows an overall increase of two orders of magnitude when compared to the lowest value of k for the same specimen. With this limited data on permeability measurements for specimen tested perpendicular to foliation plane, one could interpret that the overall k value for Cobourg limestone does not show a direct relationship to the foliation plane. Analysis of permeability data for other specimens tested perpendicular to foliation plane will help to justify this statement.

The permeability experiments carried out in this project and other projects with NWMO on Cobourg limestone give k in the range of E-19 to E-20 m^2 for intact specimen in both direction of parallel and perpendicular to foliation plane using a pressure decay of 1MPa. Radial flow permeability testing of the Cobourg limestone under transient and steady-state test methods has given similar permeability estimates (Selvadurai and Jenner, 2012). In the said investigation, the steady state experiments were performed at a constant temperature of 21 ºC for a period of 1000 to 1400 minutes with internal pressure varying from 1 to 1.4 MPa, and permeability was found to vary in the range of 1.17×10^{-20} to $1.68\ 10^{-19}$ m^2. The transient hydraulic pulse tests were conducted under the pressure pulse of 350 seconds in duration, and the permeability measured for the cavity (sealed borehole within Cobourg limestone specimens) pressure decay of 1.6 to 1.7 MPa was estimated to be between 1.3×10^{-19} and 1.5×10^{-19} m^2. In our previous experiences of testing on Cobourg limestone all the specimens show a systematic decrease of permeability (under THM conditions) as a function of heating and differential stress increments followed by an increase in permeability values responding to fracture initiation and propagation parallel to σ_1 prior to failure. This behavior was compatible with the evolution of seismic wave velocities with heating, differential stress increments, and the deformational pattern of tested specimens (Nasseri et al. 2013, Nasseri and Young, 2014).

Figure 21 shows the intact and tested photos for specimen CLV-3-T. The sketch in the same figure shows the alignment of foliation planes with 3D direction of seismic wave velocity measurements. Figures 22 to 25 shows all the seismic velocities and SWS variation of tested specimen as a function of axial stress in the same manner discussed for earlier specimens. The

overall similarity of the said properties and its variation confirms the reproducibility of these properties and the influence of inherent anisotropy existing within Cobourg limestone specimens.

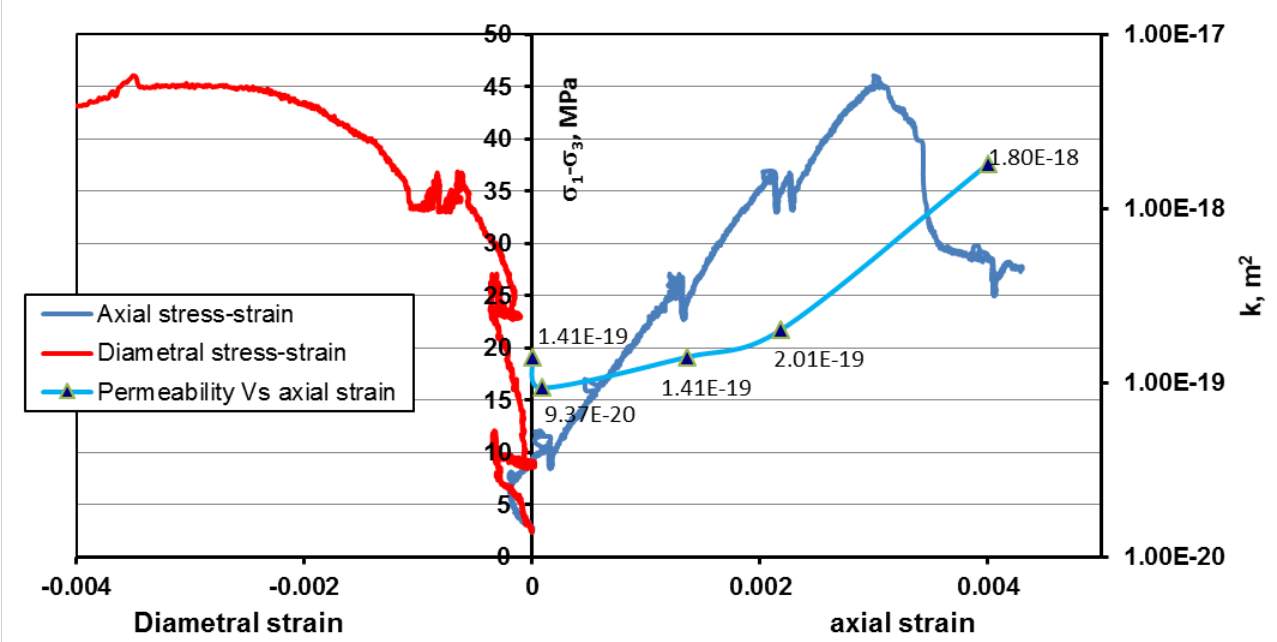

Figure 20. Variation of axial and diametral strains with differential stresses for specimen CLV-3-T tested at 5 MPa confining pressure and 3 MPa pore pressure, respectively. Variation of permeability with axial strain is shown in the figure. The hydraulic pulse was introduced from the top end of the specimen.

Figure 21 shows the specimen CLV-3-T prior and after testing. The inset sketch shows the orientation of 3D seismic velocity measurement directions with respect to foliation planes in the specimen. The failure pattern shows propagation of shear type of a failure plane diagonally cutting through the specimen. This failure pattern is different than what has been observed in the specimens with their foliation planes oriented parallel to the long axis of the specimen in which activation of foliation planes were clearly the cause of failure of the specimens.

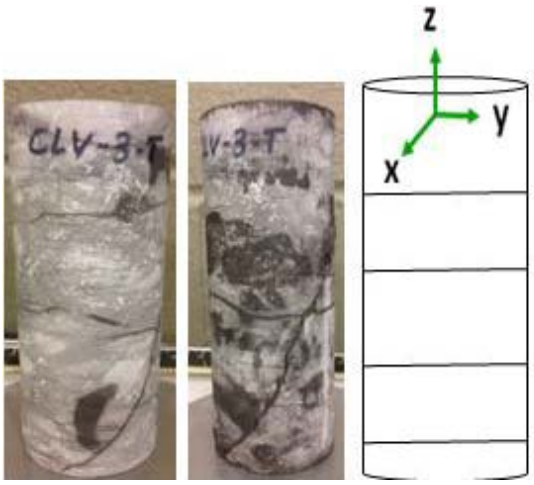

Figure 21. Comparison of failure pattern (middle image) observed for the tested specimen CLV-3-T with that of intact one (on the left). The sketch shows the 3D orientation of wave velocity measurements with respect to the foliation planes. The hydraulic pulse was introduced from top of the specimen for permeability measurements.

3.2.4.1 Evolution of ultrasonic wave velocities with differential stress increment

Figures 22 to 25 show the variation of the compressional (V_P), shear (V_{S1} and V_{S2}) seismic wave velocities and shear wave splitting (SWS) as a function of axial stress for specimen CLV-3-T. V_P continuously increases along the Z direction, which is parallel to the σ_1 loading direction up to a differential stress of 50 MPa. V_{PZ} is smaller than V_{PX} and V_{PY} initially due to the presence of foliation planes oriented perpendicular to the σ_1 loading direction involving XZ plane (Figure 22). The effect of anisotropic planes oriented parallel to the XY plane in the specimen is well documented in the evolution of the compressional better than that of shear wave velocities. V_{S1Z} shows a better improvement with initial axial loads in comparison to V_{S1X} and V_{S1Y} due to the compaction of foliation planes loaded normal to them. V_{S1X} shows a declining trend beyond 30 MPa of axial stress due to formation of axial micro-fractures parallel to σ_1 direction. SWS for this specimen is not characterized by higher values of initial percentages of splitting along XZ plane and show an initial percentage of 7% to 11% for Z and X axes respectively (Figure 25) in comparison to specimens tested parallel to foliation planes in which the initial SWS varied between 5% to 15% for the same axis (Figure 7). The initial SWS for X and Z axes measured for

specimens tested with filiation planes parallel to axial stress direction shows higher percentage of shear wave splitting due to the persistence of weak planes along the XZ plane.

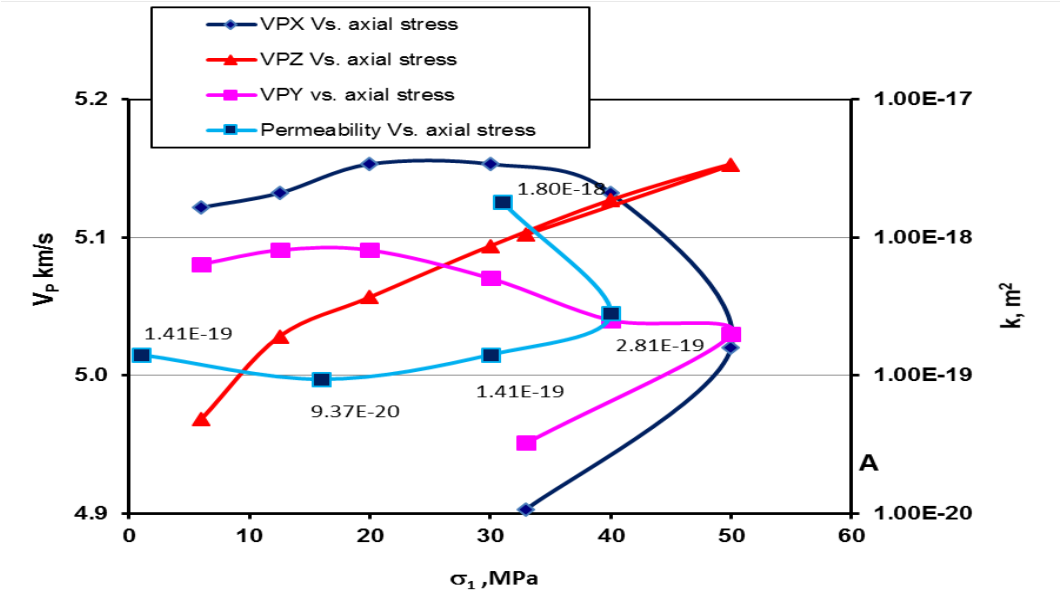

Figure 22. Variation of compressional wave velocities measured along three orthogonal axes and permeability values with axial stress for CLV-3-T specimen.

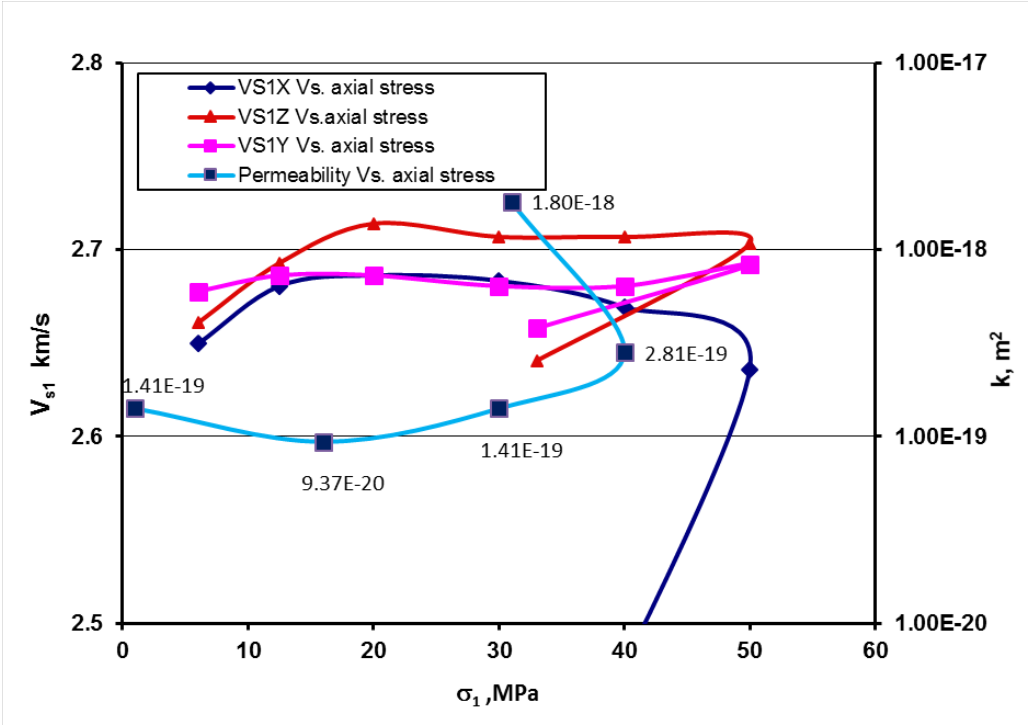

Figure 23. Variation of shear wave velocity V_{S1} and permeability as a function of axial stress.

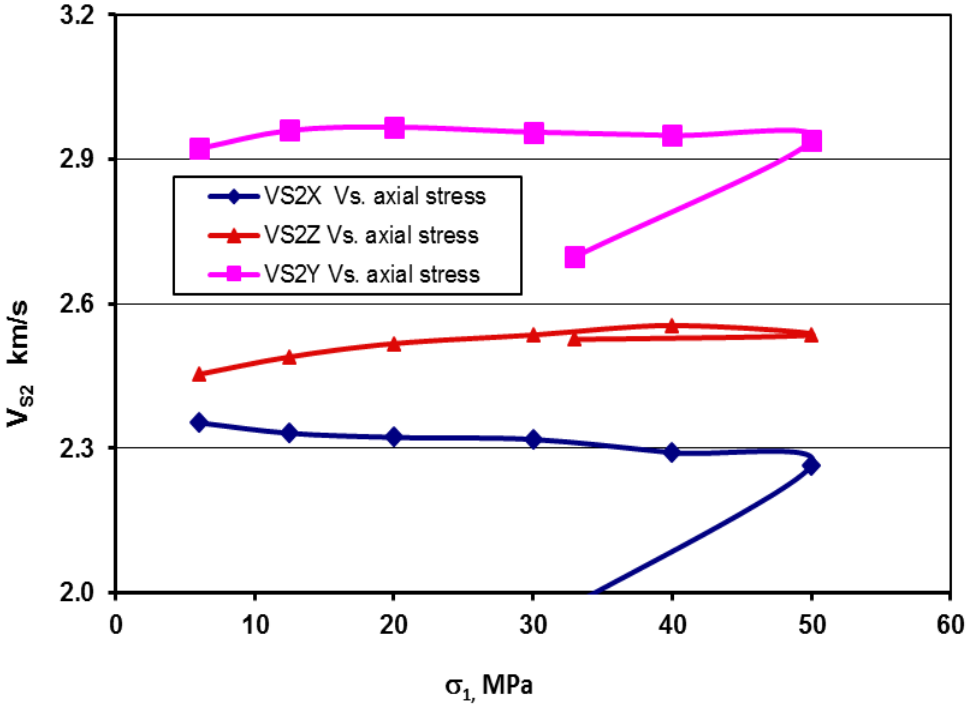

Figure 24. Variation of shear wave velocity V_{S2} as a function of axial stress.

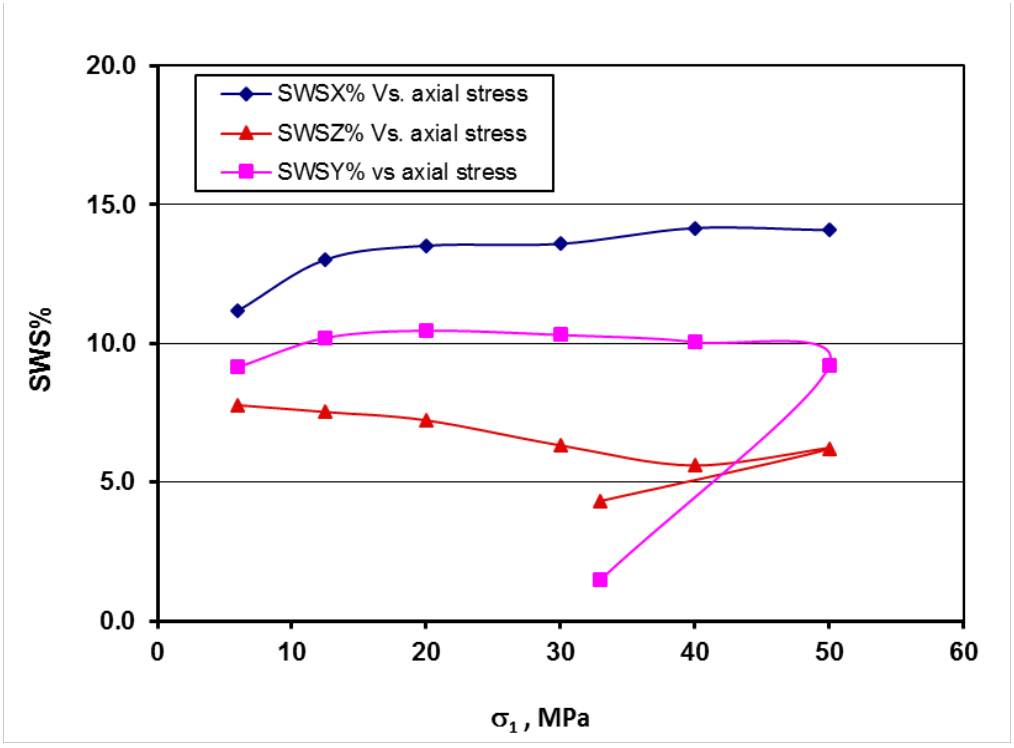

Figure 25. Variation of SWS% as a function of axial stress for specimen tested perependicaular to the folilation plane.

3.2.5 Specimen CLV-1-U (perpendicular to the foliation plane)

Figure 26 shows the variation of axial, diametral strains and permeability values of differential stresses up to failure and into the post-failure regime for this specimen. Specimen CLV-1-U failed at 56 MPa of axial stress, experiencing 0.65% and 0.32% of axial and diametral strain, respectively. Figure 27 shows the failure pattern of the specimen after the test in comparison with the specimen's intact image shown on the left side. The sketch in Figure 27 shows the 3D orientation of the foliation plane with respect to the long axis of the specimen and the direction for wave velocity measurements within the cell.

The permeability of specimen CLV-1-U was measured at 1.8 MPa of differential stress and was found to be 1.41E-19 m^2 and the variation of the permeability is shown as a function of axial strain in the secondary vertical axis in Figure 26. The k value for CLV-1-U decreased to 4.6E-20 m^2 and then increased to 5.6E-19 m^2 and 8.6E-18 m^2 as the axial stresses were raised up to 31 MPa and 45 MPa, respectively, reflecting the initial compaction followed by the initiation of fracturing. The k value measured, almost near peak stress, shows that the k increased almost two orders of magnitude, which is related to the generation of micro-fractures during the pre-peak strength of the specimen tested. The post failure k was found to be 1.87E-19 m^2.

In this experiment we did not observe an increased k value for post failure stress. This observation could be due to factors such as: the interaction of failure planes in the specimen with the top loading platen; and the spatial coincidence between the water distribution ring in the platen from where the hydraulic pulse is sent and the failed surfaces in the specimen. Formation of gouge material and its effect on the reduction of permeability could be another reason for such observation. These values of k and their evolution as a function of axial stresses are in good agreement with the earlier investigation RFDF carried out in a separate research on the THM properties of Cobourg limestone (Nasseri et al., 2012; Nasseri et al., 2013). Radial flow permeability testing of the Cobourg limestone measured under transient, and steady-state test methods have given similar permeability estimates as reported by Selvadurai and Jenner (2012).

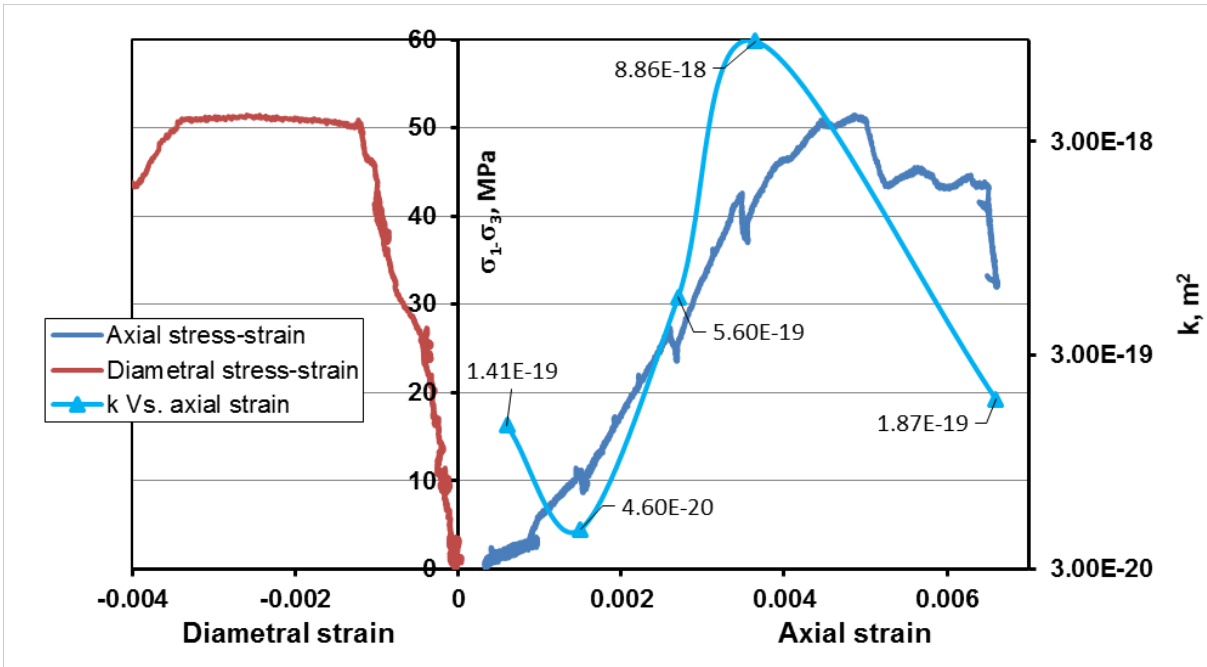

Figure 26. Variation of axial and diametral of strains with differential stresses for CLV-1-U specimen tested at 5 MPa confining pressure and 3 MPa pore pressure, respectively. Variation of log k with axial strain is shown. The hydraulic pulse was introduced from the top end of the specimen.

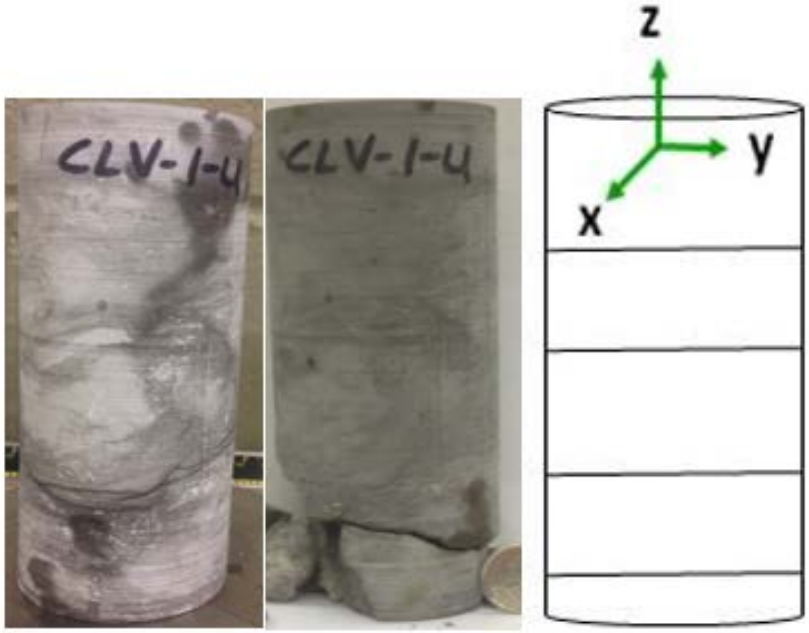

Figure 27. Failure pattern observed for the specimen CLV-1-U is shown. The sketch shows the 3D orientation of wave velocity measurements with respect to the foliation planes.

3.2.5.1 Evolution of seismic wave velocities with differential stress increment, CLV-1-U

The V_P continuously increases along the Z direction, which is parallel to the σ_1 direction up to a differential stress of 50 MPa. The V_P measured along two horizontal directions (X and Y) initially showed a slight increase up to a differential stress of 20 MPa, followed by a slight decrease to a differential stress of around 45 MPa where a large decrease occurs (Figure 28). Figures 29 and 30 show the shear wave velocity V_{S1} and its polarization (V_{S2}) as a function of axial stress along three perpendicular directions (X, Y, and Z axes) for the CLV-1-U, respectively. In this specimen foliation planes are running parallel to the XY plane and the Z axis is perpendicular to the XY plane (sketch in Figure 27). Along the σ_1 direction (Z axis), V_{S1Z} and V_{S2Z} show higher increments of velocity than the other two horizontal directions due to the closure of foliation planes responding to the compressional stresses along Z axis. Variation of shear wave velocities along the two horizontal axes of X and Y (Figures 4 and 5) can be related the heterogeneity of the matrix along the XY plane in Cobourg limestone.

Figure 31 shows the shear wave splitting (SWS) and its variation measured along three directions as a function of axial stress increments. The SWS along the Z axis is progressively reduced with the axial stress increments, which reflects on the suppression of the anisotropic nature of the specimen and thus the effect of the horizontally oriented weak planes (parallel to XY plane) on the shear velocity changes. The progressive increase of SWS along both the X and Y axes indicates nucleation and propagation of axial micro-fractures parallel to the Z axis prior to sample failure.

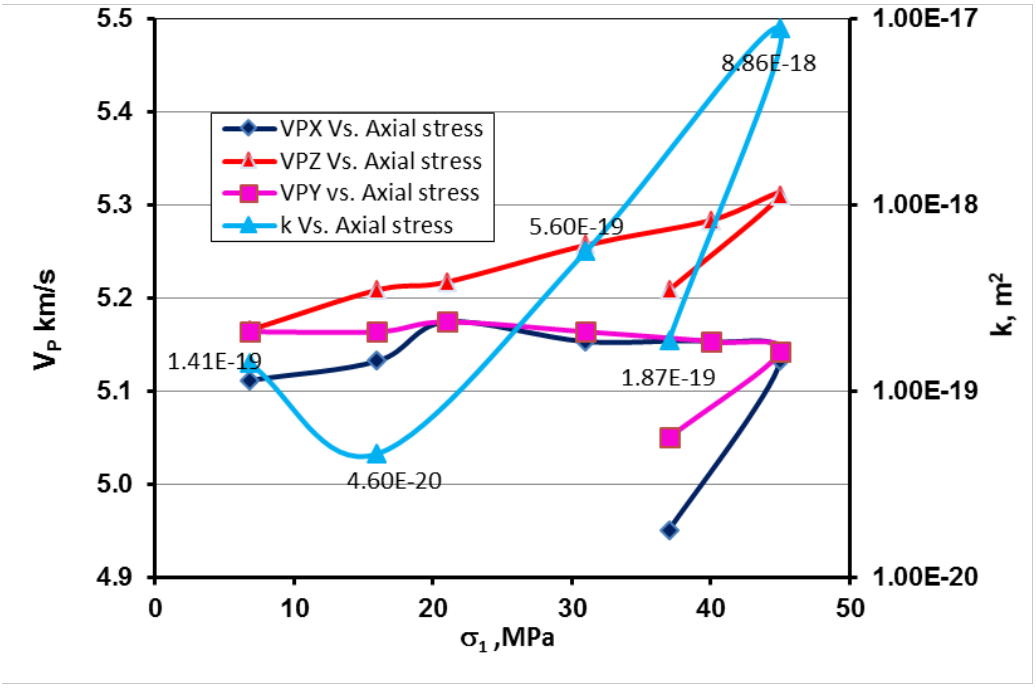

Figure 28. Variation of compressional wave velocities measured along three orthogonal axes and log. The k values with axial stress for the CLV-1-U specimen.

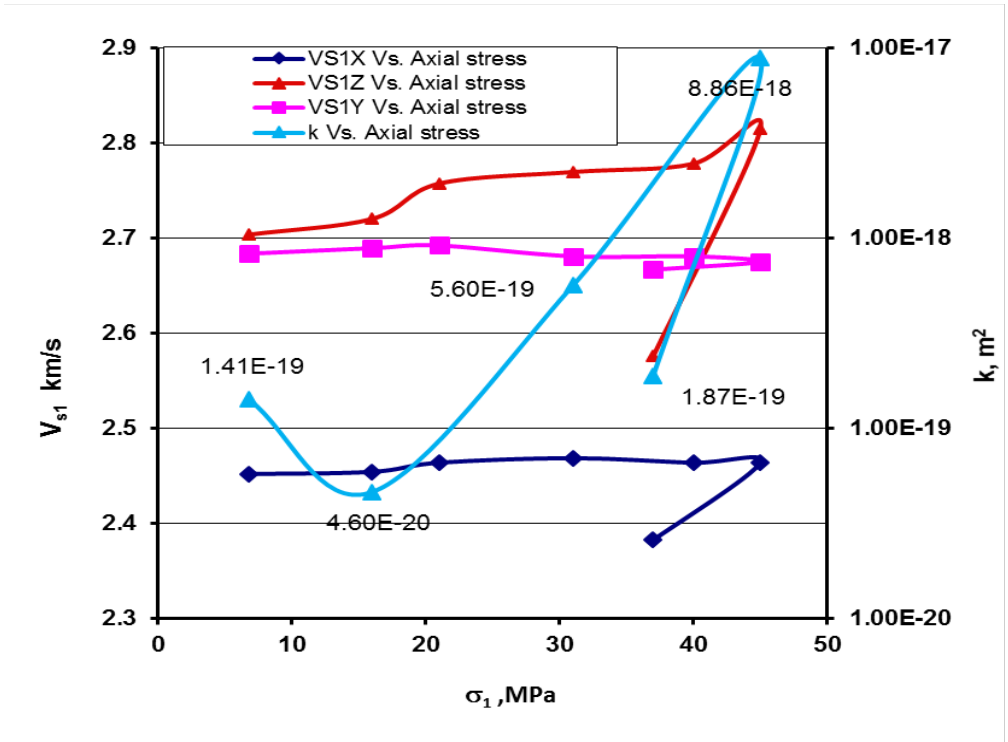

Figure 29. Variation of shear wave velocity in V_{S1} and log k values as a function of axial stress.

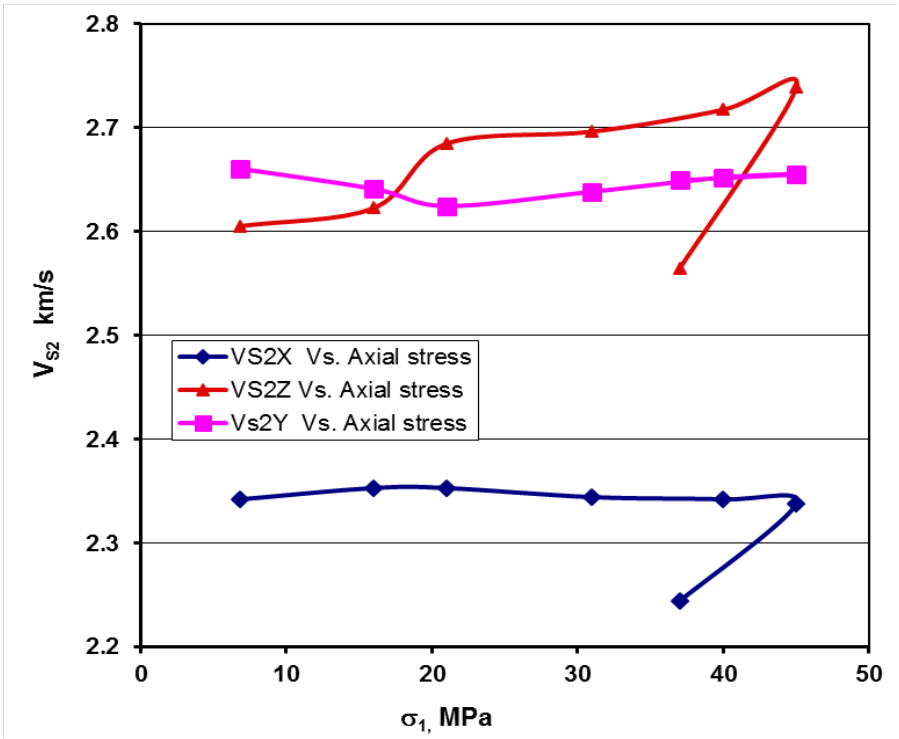

Figure 30. Variation of shear wave velocity V_{S2} as a function of axial stress.

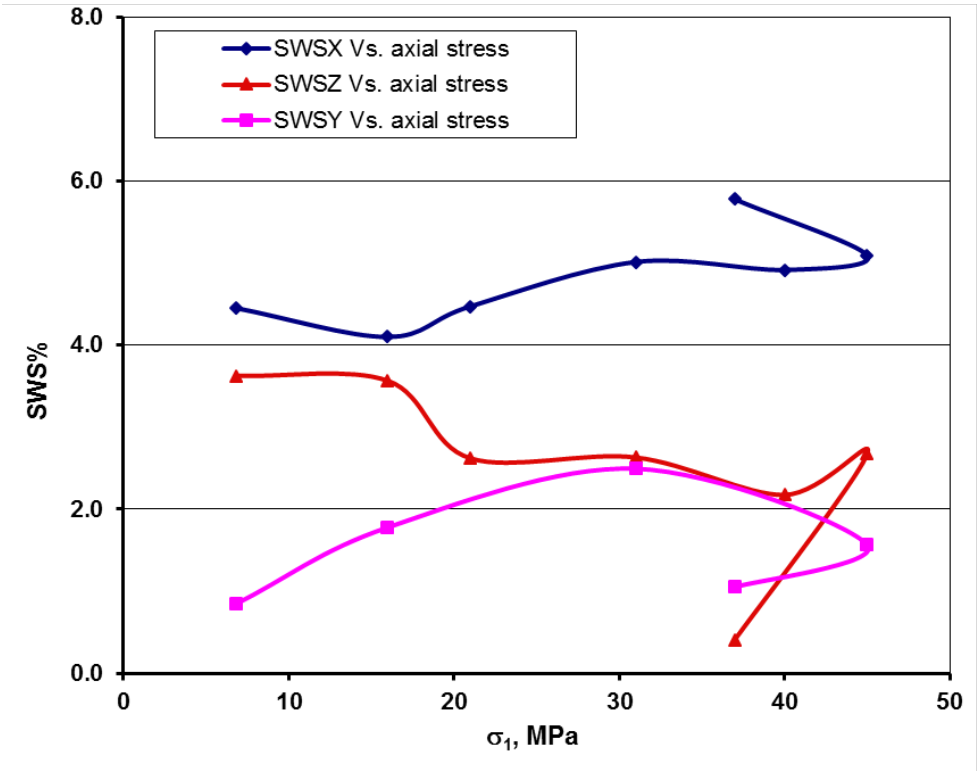

Figure 31. Variation of SWS as a function of axial stress for CLH-3-T.

3.2.6 Specimen CLV-5-T (perpendicular to foliation plane)

Figure 32 shows the variation of axial strains at various differential stresses up to and beyond failure for specimen CLV-5-T tested under a similar testing procedure established during the first experiment. Herein k as a function of axial strain is shown in the same graph in the second vertical axis. This specimen failed at 46 MPa of differential stress with an axial strain of 1.2%.

The overall trend of permeability measured for this specimen follows a similar path as that of specimen CLV-1-U with the exception that the current specimen's post peak k shows almost the same value as the initial permeability measured at 5 MPa of hydrostatic stress.

The measured initial k value was reduced in one order of magnitude when the specimen was in its elastic state. The severity of the post failure damage (Figure 33) is further manifested by the seismic wave velocity changes in the tested specimens. This will be discussed in the next section. Figure 33 shows the failure pattern of the tested specimen and a sketch of the specimen with its foliation plane orientation with respect to the 3D direction of wave velocity measurements.

Figure 2 and Figure 3 in Appendix A show the images of various sections and mosaics of the thin section images for the two specimens of CLH-3-T and CLV-3-T. The permeability value measured for specimen CLH-3-T at post failure stress shows a reduction of k from 8.91E-19 m^2 (measured prior to failure) to 1.4E-19 m^2. Whereas the post failure k value measured for specimen CLV-3-T shows an increase from 2.01E-19 m^2 (measured prior to failure) to a value of 1.8E-18 m^2. One would expect to see that the post failure k for specimen CLH-3-T should be much higher than its k value measured prior to the failure due to the numerous fractures observed at the top slices of specimen CLH-3-T. However, the measured data did not show this relationship. The situation is reverse for specimen CLV-3-T. Therefore based on limited number of specimens processed for thin section studies (one for each direction), a direct correlation between the post peak k values and the spatial distribution or number of observed fractures in the thin sections for the two specimens mentioned above could not be established in this study.

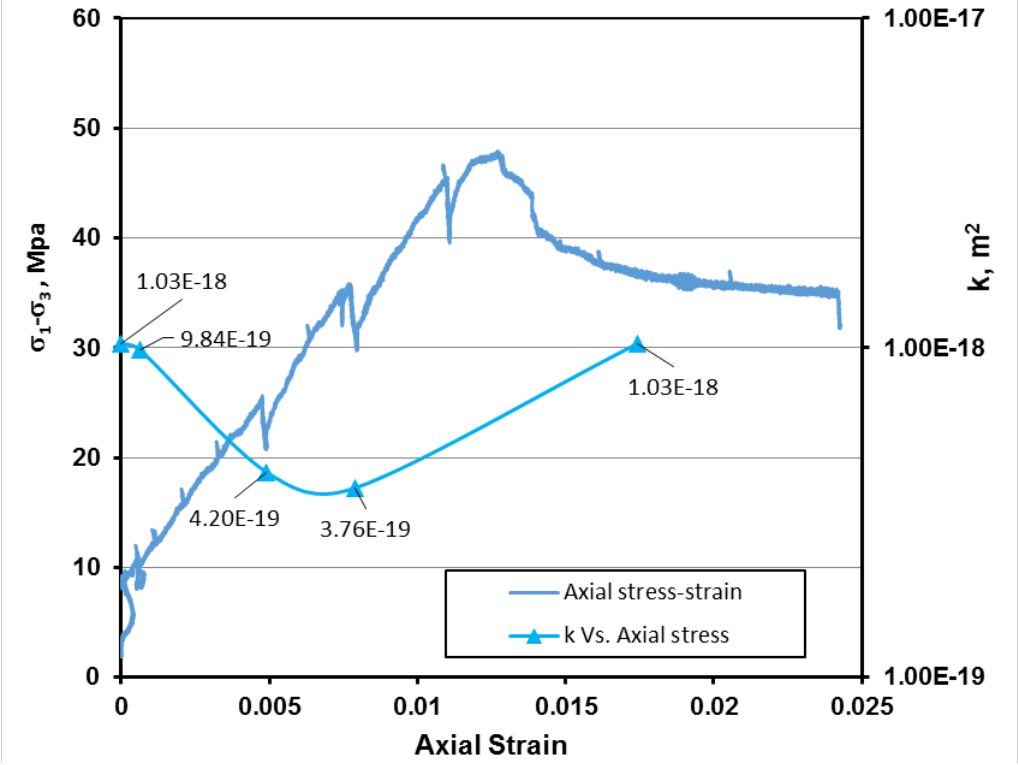

Figure 32. Variation of differential stress with axial strain for specimen CLV-5-T tested at 5 MPa and 3 MPa of confining and pore pressures, respectively. K as a function of axial strain is shown as the second vertical axis. The hydraulic pulse was introduced from top of the specimen.

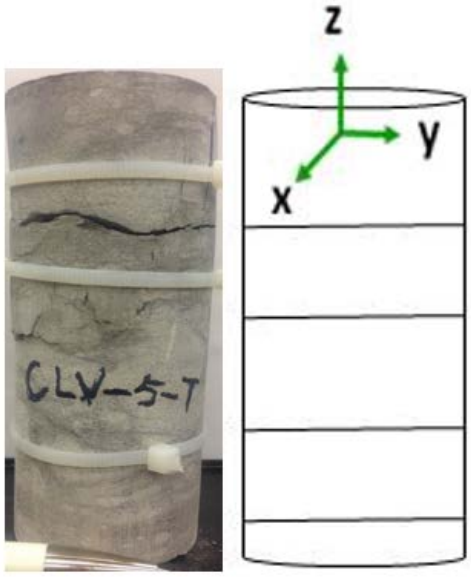

Figure 33. Failure pattern observed for the tested specimen CLV-5-T. The sketch shows the 3D orientation of wave velocity measurements with respect to the foliation planes (The larger horizontal fracture in the sample was caused during recovery of the specimen from the cell and is not a part of failure pattern).

3.2.6.1 Evolution of ultrasonic wave velocities with differential stress increment, CLV-5-T

Figures 34 to 37 show the variation of the compressional (V_P), shear (Vs1 and Vs_2) seismic wave velocities, and shear wave splitting (SWS) as a function of axial stress for specimen CLV-5-T.
A similar trend to that of the earlier specimen is observed for the specimen CLV-5-T, showing the reproducibility of seismic properties in the specimens tested perpendicular to the foliation planes. The V_P continuously increases along the Z direction, which is parallel to the σ_1 direction up to a differential stress of 46 MPa. The V_{PY} and V_{PX} show a declining profile (Figure 34) due to the formation of micro-fractures parallel to the σ_1 direction. The effect of anisotropic planes oriented perpendicular to the XY plane in the specimen is well documented in the behaviour of the two horizontal shear wave velocities that are oriented at polarized directions. The V_{S1Y} shows an initial higher value than V_{S1Z}, which may reflect a faster shear wave velocity along the Y axis within the XY plane of symmetry.

Figure 37 shows SWS as a function of axial stress, measuring the anisotropic nature of the Cobourg limestone being tested with the foliation planes perpendicular to the axial stress direction. The SWS for the X and Y axes shows a higher degree of anisotropy due to the presence of XY weak planes.

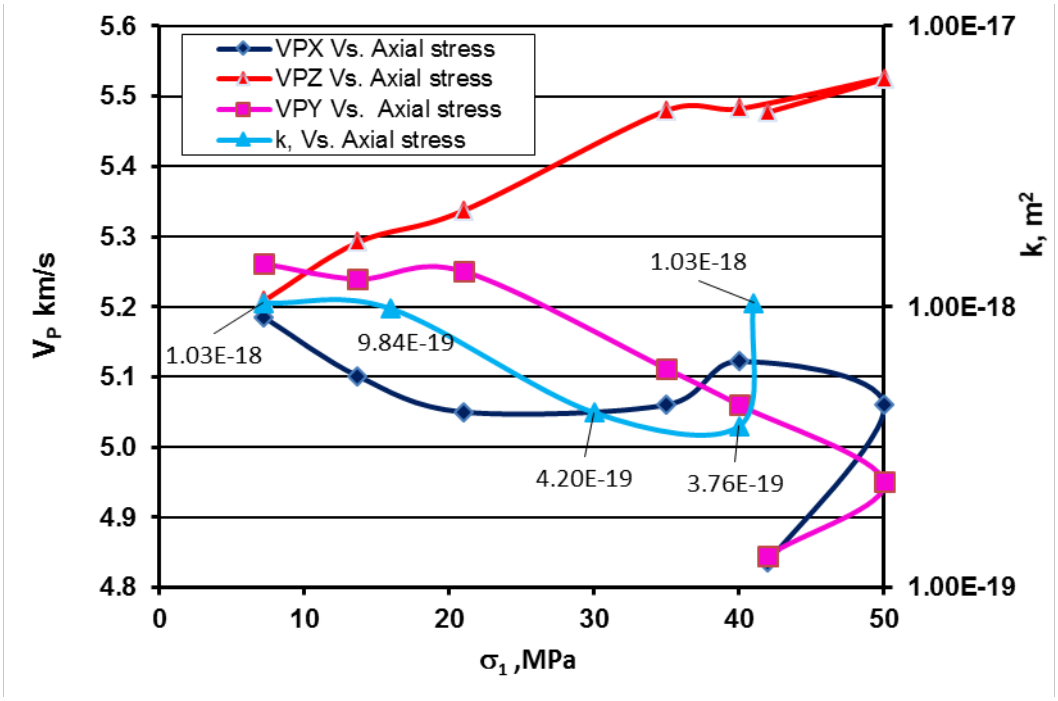

Figure 34. Variation of compressional wave velocities measured along three orthogonal axes and permeability (log k) with axial stress for the CLH-5-T specimen.

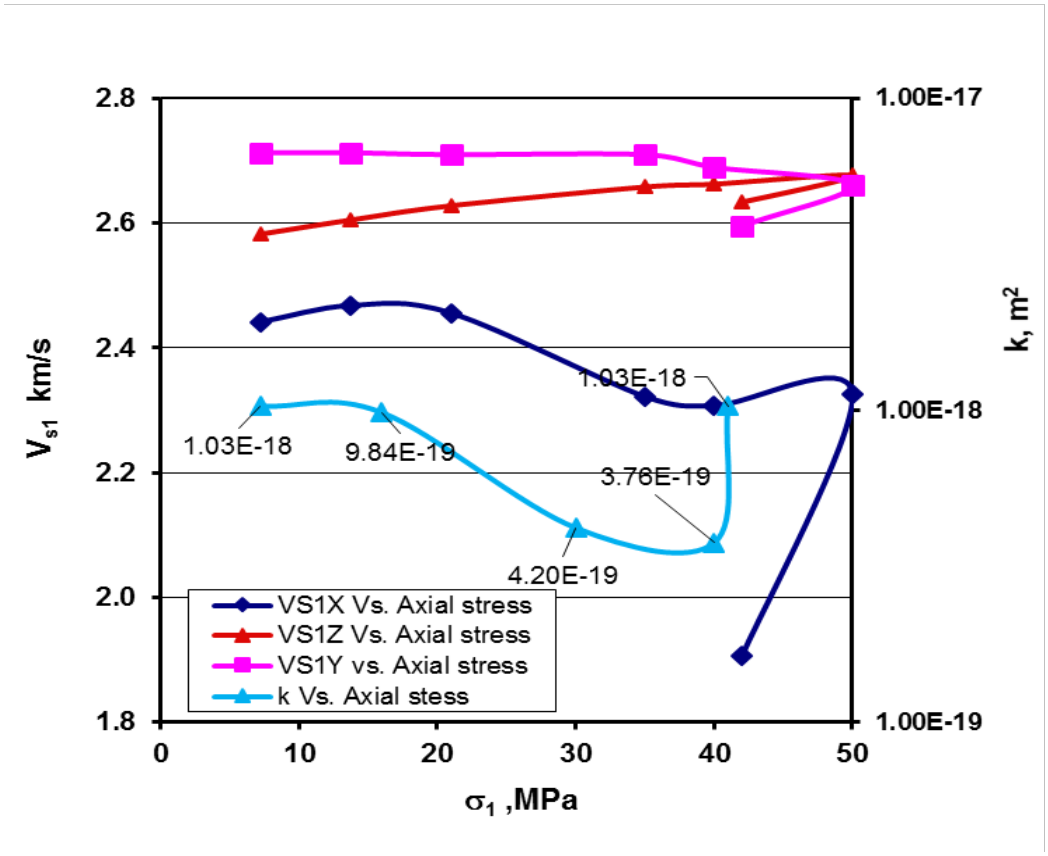

Figure 35. Variation of shear wave velocity V_{S1} and permeability as a function of axial stress.

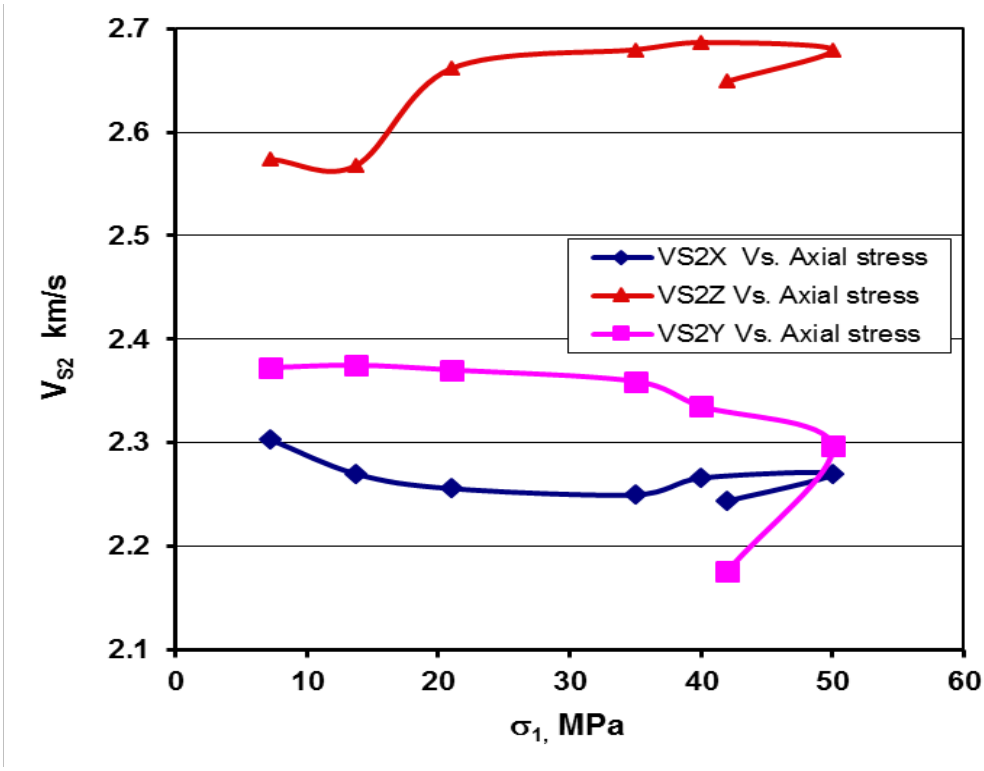

Figure 36. Variation of shear wave velocity V_{S2} as a function of axial stress.

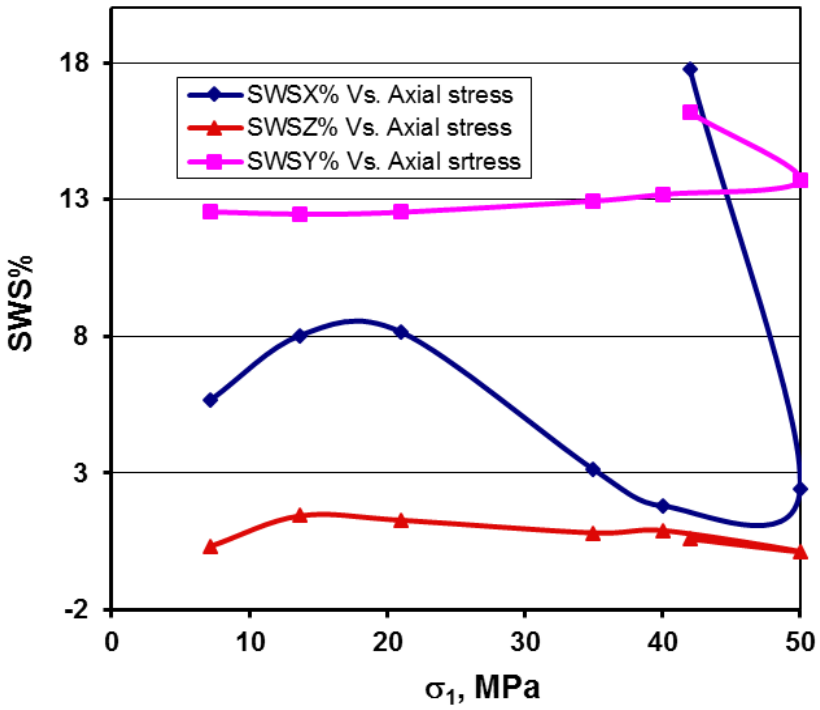

Figure 37. Variation of SWS as a function of axial stress for CLV-5-T.

4 Experiment for Tournemire Shale

4.1 Testing procedure for Tournemire shale tested under 30 minutes of saturation

1. Gradually bring the axial and confining pressure (lateral) to 5 MPa on the specimen.
2. Create 2 MPa of pore water pressure on the top and bottom of the specimen in the cell and regulate it. Both top and bottom pore pressure sensors attached to top and bottom platens detect 2 MPa regulated by the quizix pump working as independent pistons.
3. Close the bottom valve connected to the quizix pump that was regulating 2 MPa of pore water pressure to the bottom of the specimen.
4. Create 1 MPa extra pore pressure as a pulse (total of 3 MPa) on top of the specimen while the bottom valve is closed.
5. Close the top valve as soon as pore water pressure reached 3 MPa (sensed by the additional pore water pressure sensor close to the specimen on top platen).
6. Start logging the water pressure data from the top and bottom pore pressure sensors close to the top and bottom of the specimen to collect the decaying pulse from the top of the specimen with time. This parameter is then used to calculate permeability of the specimen at that state of initial hydrostatic stress or very small differential stress, and at various differential stresses.
7. Increase the axial load to a new σ_1 stress and stop the load and repeat the same steps described in steps 3 to 6. During the axial loading, while σ_3 is regulated at 5 MPa, the top and bottom of the specimen are exposed to pore water pressure regulated at 2 MPa.
8. Continue measuring permeability of the specimen a few times before failure and once after failure.
9. Wave velocities are measured along all three axes at constant axial loading intervals.

4.2 Testing results for Tournemire shale tested under 30 minutes saturation

4.2.1 Specimen TS0°-1 (parallel to the bedding planes)

One specimen of the Tournemire shale (TS0°-1) with 0° orientation to the bedding planes has been tested following the testing procedure mentioned above. It failed at 50 MPa of σ_1 with

0.95% of axial deformation at peak strength (Figure 38). Permeability values are shown in Figure 38 for four differential stress levels for specimen TS0^o-1. The permeability at 2.3 MPa of differential stress was measured near 3.17E-19 m^2 and it was slightly reduced when measured at the next differential stress of 5 MPa due to an initial compaction effect. The k value for specimen TS0^o-1 increased to 4.2E-18 m^2 (an order of magnitude higher) when axial stress was raised to 24 MPa and then slightly decreased to 2.7E-18 m^2 when measured at 40 MPa. Shearing along the failure plane and creation of gouge materials could be responsible for reduction of the k value in this specimen. Figure 39 shows the failure pattern along with the orientation of the weak planes in the 3D sketch that is drawn with respect to the long axis of the specimen along which the wave velocities were measured in the cell. The XZ plane defines a plane parallel to the weak foliation planes. There are numerous axial long fractures which are observed to coincide with the aforementioned plane of symmetry (i.e. EZ plane).

4.2.1.1 Evolution of ultrasonic wave velocities with differential stress increment, TS0°-1

Figures 40 to 43 show the variation of the compressional (V_P), shear (Vs1 and Vs_2) seismic wave velocities, and shear wave splitting (SWS) as a function of axial stress for specimen TS0^o-1. The V_P continuously increases along the Z direction, which is parallel to the σ_1 direction up to an axial stress of 47 MPa.

The V_{PZ} and V_{PX} show a higher value (Figure 40) than V_{PY} due to the way the specimen was placed in the cell with respect to the 3D orientation of the V_P sensor in the cell. The Y axis in the cell is oriented normally to the XZ plane of the specimen. Orientation of specimen's pre-existing foliation planes indicates that they have a similar effect on shear wave velocities to that of the compressional wave velocity when evaluated with respect to the XZ plane. The two shear wave velocities propagated normally to each other (Figures 41 and 42), i.e., the V_{S1Y} and V_{S2Y} are both much slower than the other two shear velocities propagating along the Z and X axes. Figure 43 shows SWS as a function of axial stress, measuring the anisotropic nature of the Tournemire specimen, TS0^o-1. The SWS for the X and Z axes indicates a higher degree of anisotropy as a function of axial stress due to the presence of a XZ weak plane of symmetry.

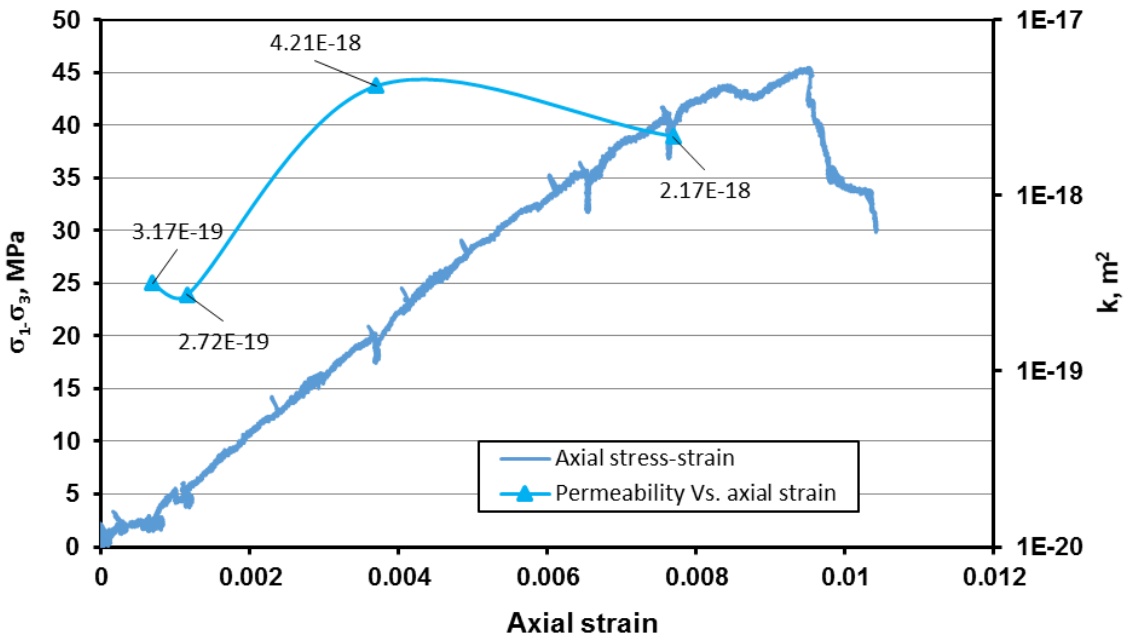

Figure 38. Variation of differential stress with axial strain for specimen TS0°-1 tested at 5 MPa confining and 3 MPa pore pressures, respectively. Permeability, k as a function of axial strain is shown on the second vertical axis. The hydraulic pulse was introduced from the top end of the specimen.

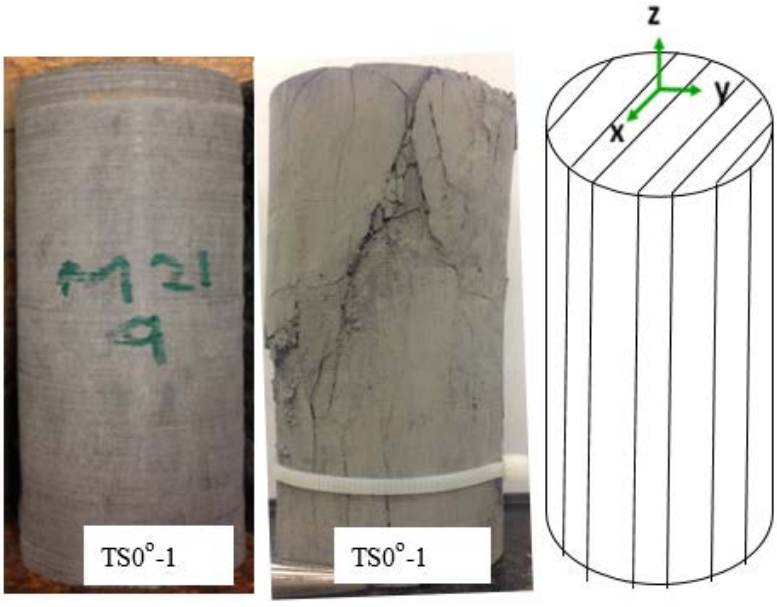

Figure 39. Failure pattern observed for the specimen TS0°-1 showing numerous axial fractures oriented parallel to the XZ plane in this specimen. The sketch shows the 3D orientation of wave velocity measurements with respect to the bedding planes.

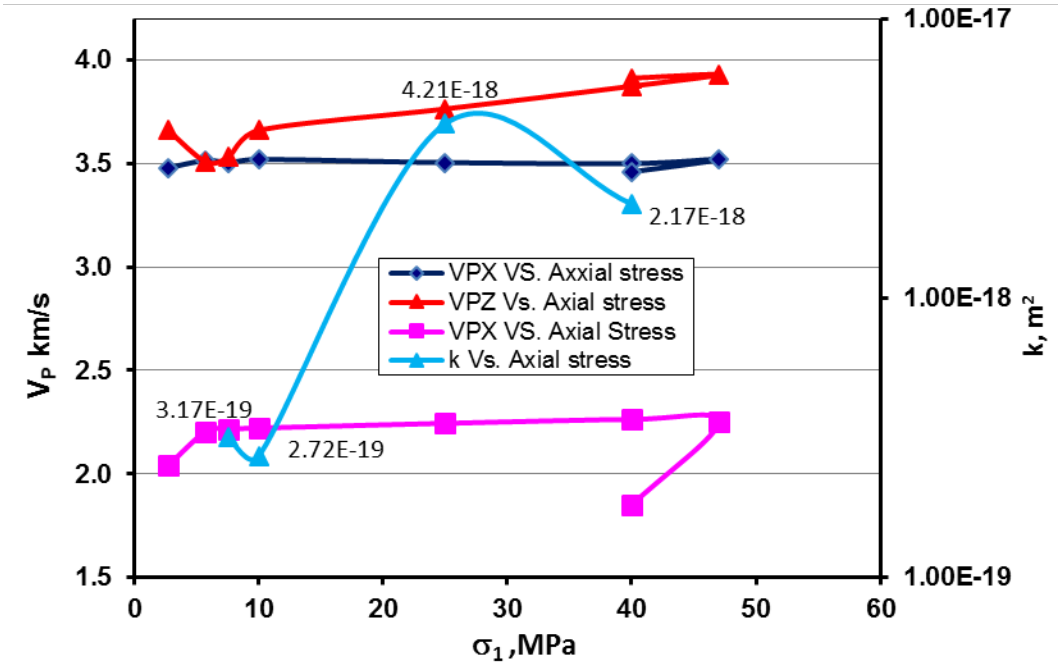

Figure 40. Variation of the compressional wave velocities measured along the three orthogonal axes and permeability with axial stress for the TS0°-1 specimen.

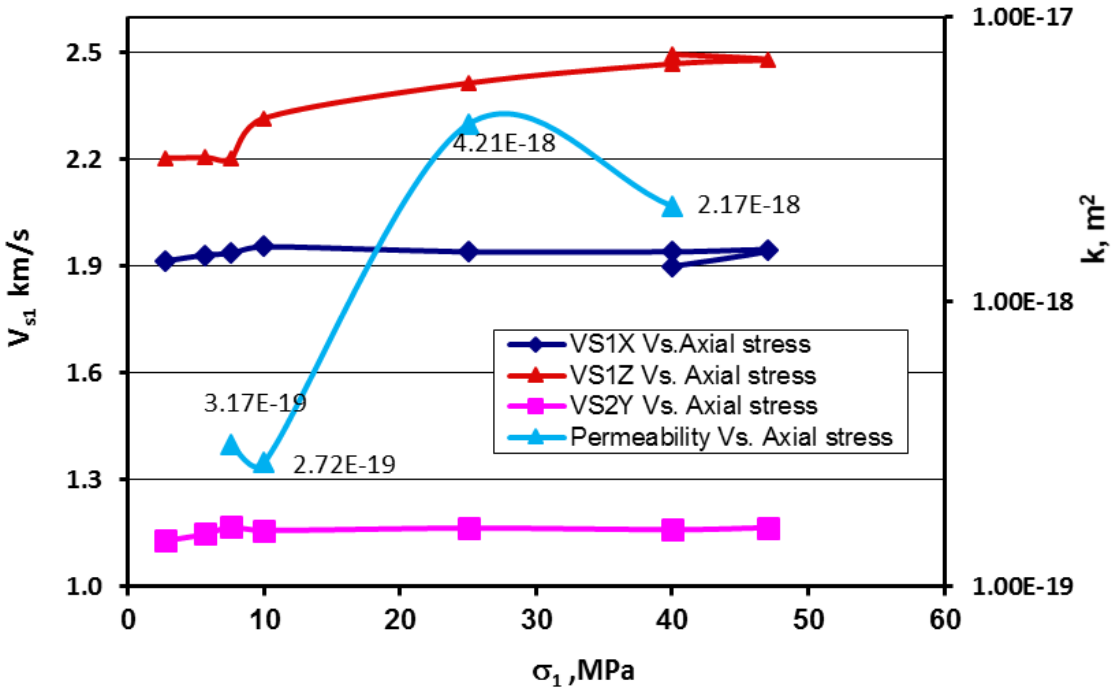

Figure 41. Variation of shear wave velocity V_{S1} and permeability as a function of axial stress.

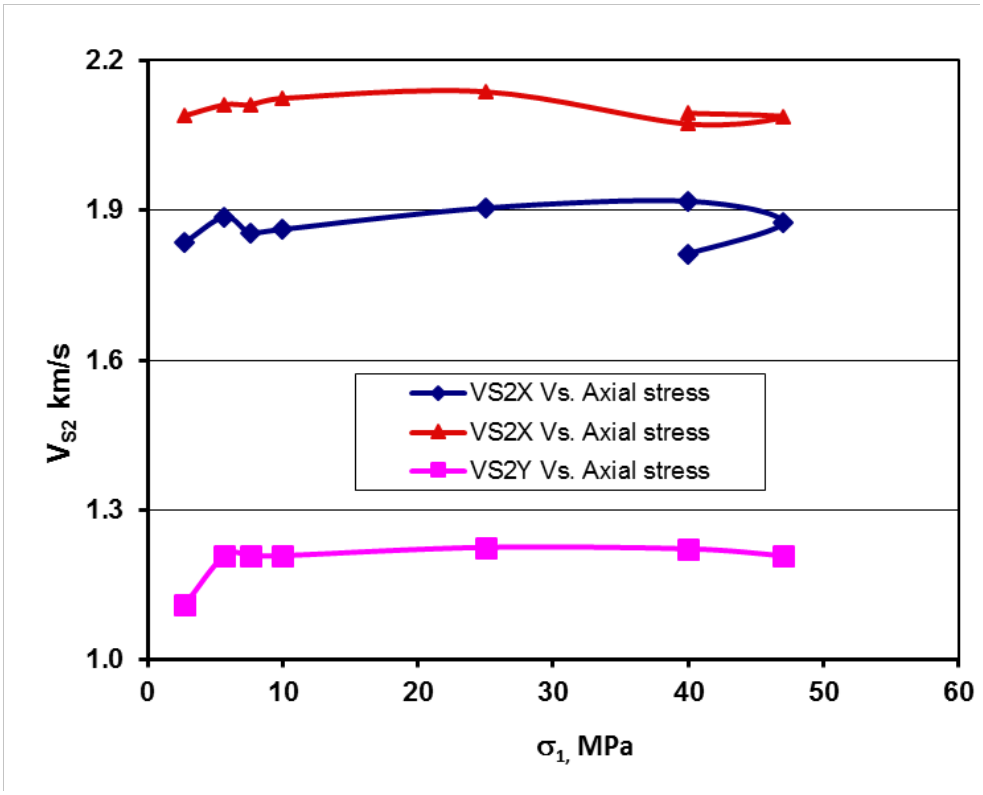

Figure 42. Variation of shear wave velocity V_{S2} as a function of axial stress.

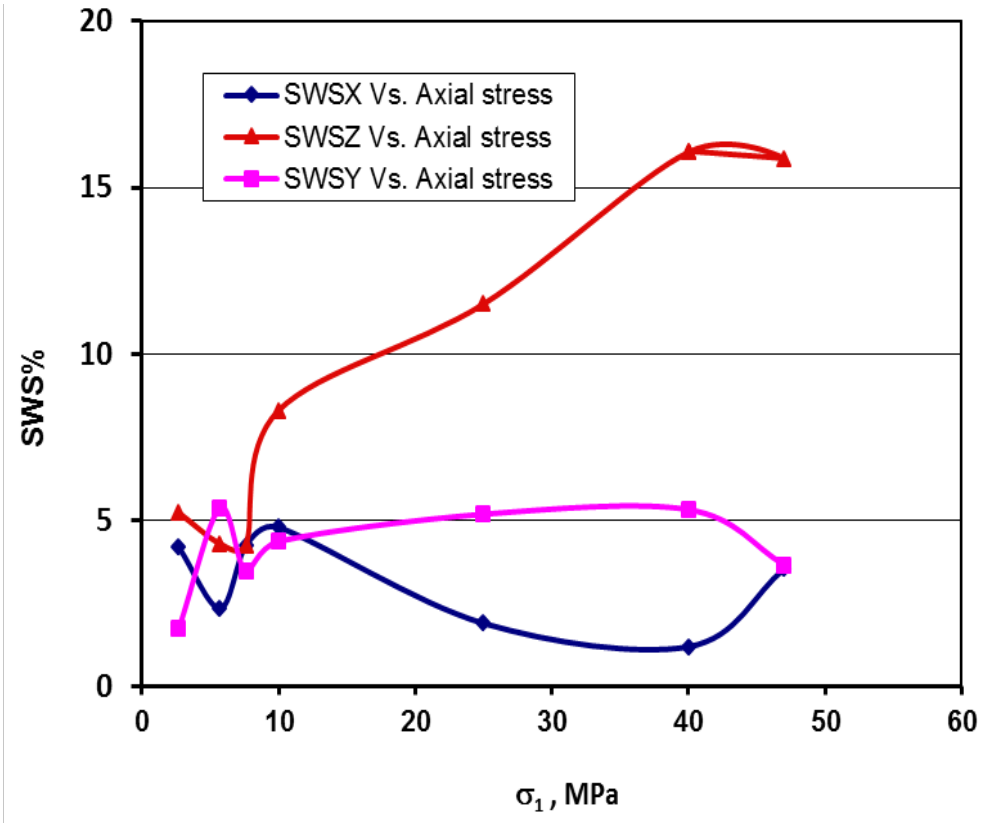

Figure 43. Variation of SWS as a function of axial stress for specimen TS0°-1.

4.2.2 Specimen TS-45°-1

Figure 44 shows the variation of axial and diametral strains as a function of differential stress for the Tournemire shale specimen (TS-45^o-1) prepared with its foliation plane oriented at 45^o with respect to the σ_1 direction. This specimen was placed into the geophysical imaging cell keeping the Y and Z wave velocity measurement axes at 45^o to the strike of the foliation plane and was tested applying a similar testing procedure to that of specimen TS0^o-1. Specimen TS-45^o-1 failed at 44 MPa of axial stress showing axial and diametral strains of 0.63% and 0.3%, respectively, at peak strength. Permeability (k) was measured at five different differential stresses for this specimen. Unlike the specimen TS0^o-1, the variation of k as a function of differential stress shows a continuous decline with respect to the initial k value measured at l MPa of differential stress. Mobilization of shear planes oriented with respect to the σ_1 direction and generation of gauge material along the mobilized weak plane could be a possible explanation of a continuous decrease in the k value in comparison to what has been observed in specimen TS0^o-1 for which the permeability was measured parallel to the XZ weak planes. Figure 45 shows the failure pattern in specimen TS-45^o-1 indicating the fractures are aligned with respect to the pre-existing weak foliation planes at 45^o with respect to the σ_1 direction.

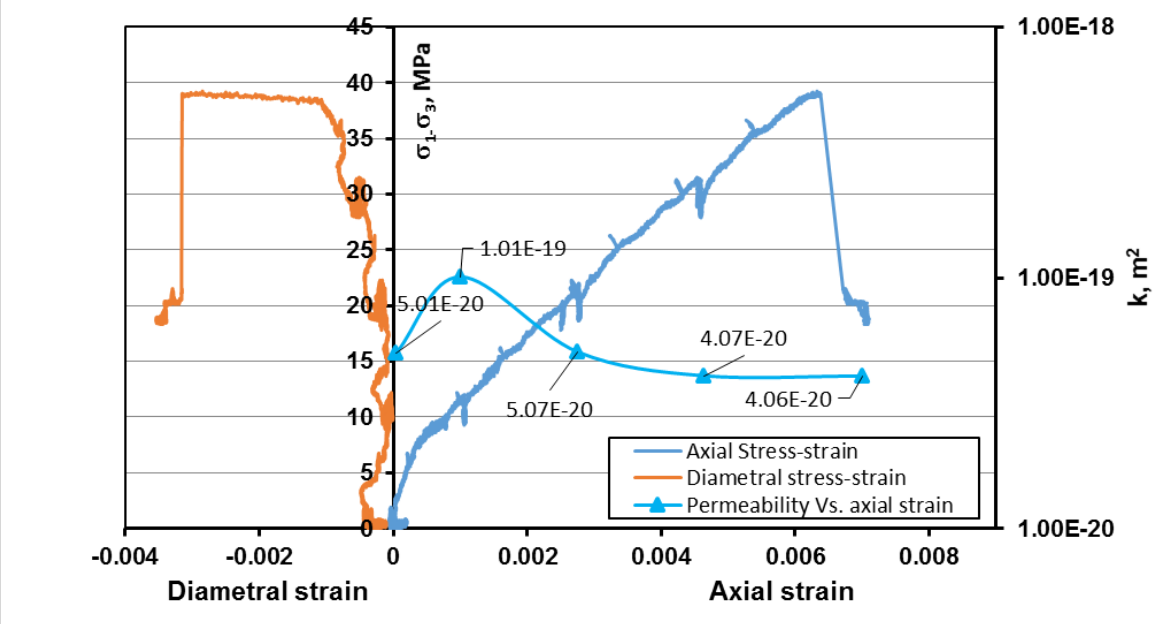

Figure 44. Variation of the axial and diametral strain with differential stress for specimen TS-45^o-1 tested at 5 MPa confining and 3 MPa pore pressures, respectively. Permeability, k (log. values) as a function of axial strain is shown on the second vertical axis. The hydraulic pulse was introduced from the top end of the specimen.

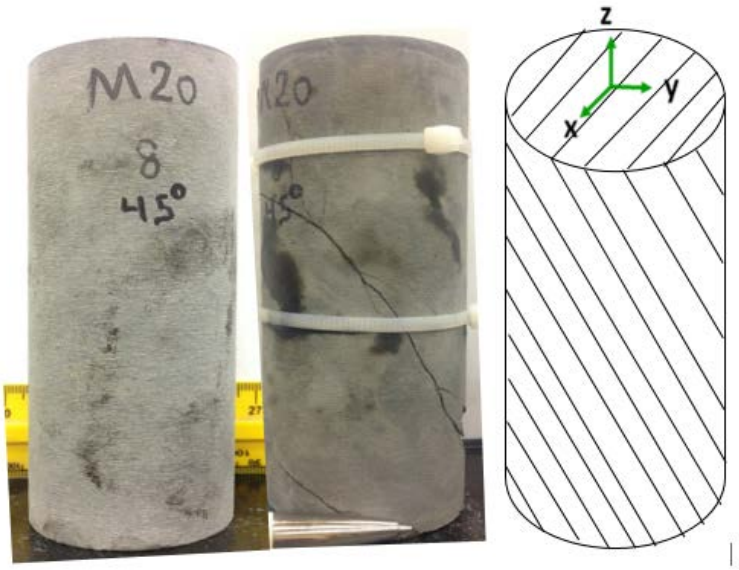

Figure 45. Failure pattern observed for specimen TS-45^{o}-1 showing failure fractures parallel to the oriented weak planes in the specimen. The sketch shows the 3D orientation of wave velocity measurements with respect to the bedding planes.

4.2.2 Evolution of ultrasonic wave velocities with differential stress increment, TS-45^{o}-1

Unlike the specimen tested at 0° orientation, the V_{PX} is higher than V_{PZ} and V_{PY} at the initial stages of axial loading. This is due to the fact that V_{PX} is measured along the strike of the foliation planes where V_{PZ} and V_{PY} are measured at 45^{o} with respect to the weak planes (Figure 46). Axial compressive stresses influence the V_{PZ} at a higher rate than V_{PX} (Figure 46). The V_{PY} is characterized with a much lower velocity due to the fact that V_{PY} is measured at 45^{o} to the foliation planes and this direction is only affected with a 5 MPa of lateral confining pressure in comparison to the axial Z direction. Orientation of the specimen's pre-existing bedding planes demonstrates a similar effect on shear wave velocities to that of the compressional wave velocity when evaluated with respect to the symmetrical plane. Both the Vs_{X1} and Vs_{X2} shear wave velocities propagating along the strike of foliation planes were shown to be higher than the shear wave velocities measured along two other directions (Figures 47 and 48).

Figure 49 shows SWS as a function of axial stress, measuring the evolution of the anisotropic nature of Tournemire specimen TS-45^{o}-1. The SWSY shows more or less as a constant value of SWS where as SWSX declines and SWSZ increases with axial stress, respectively.

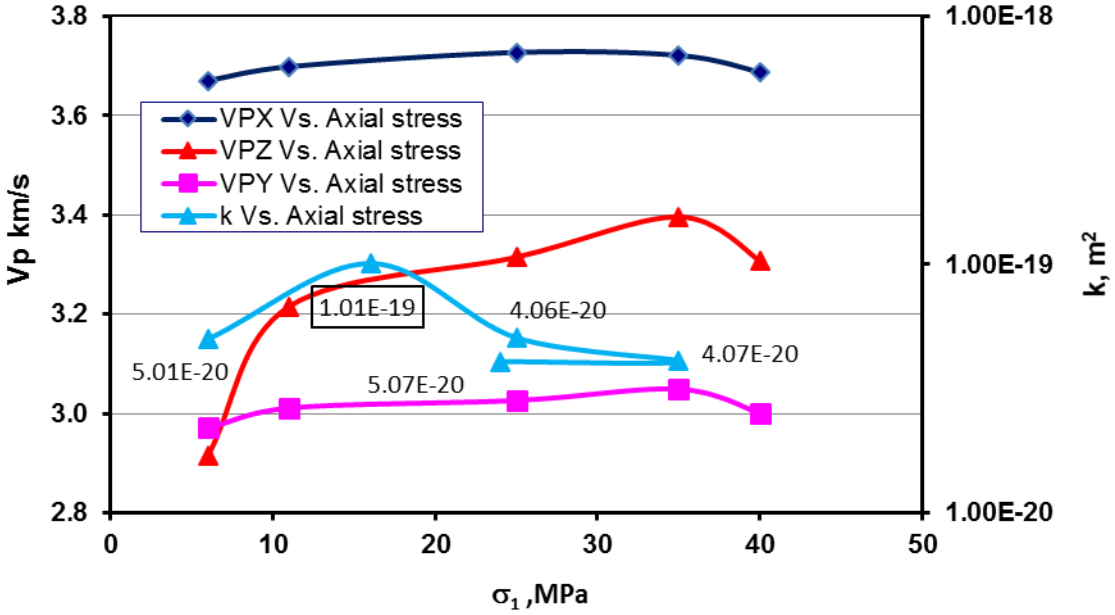

Figure 46. Variation of compressional wave velocities measured along three orthogonal axes and permeability (log. values) with axial stress for the TS-45^{o}-1 specimen.

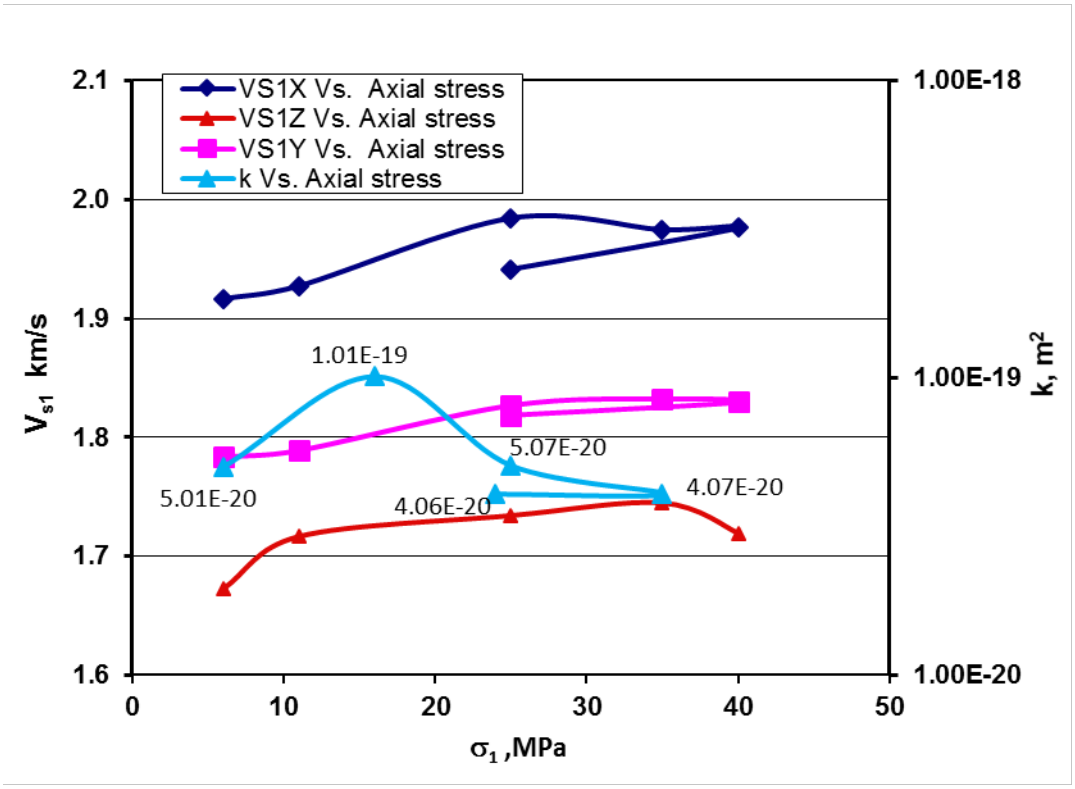

Figure 47. Variation of shear wave velocity V_{S1} and permeability as a function of axial stress.

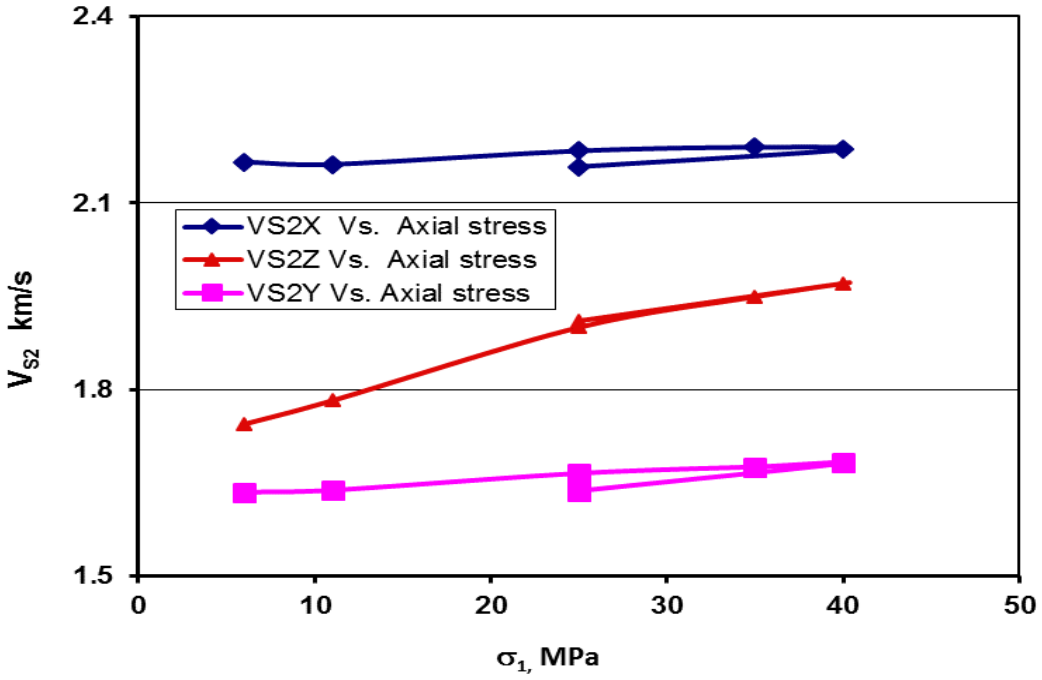

Figure 48. Variation of shear wave velocity V_{S2} and permeability as a function of axial stress.

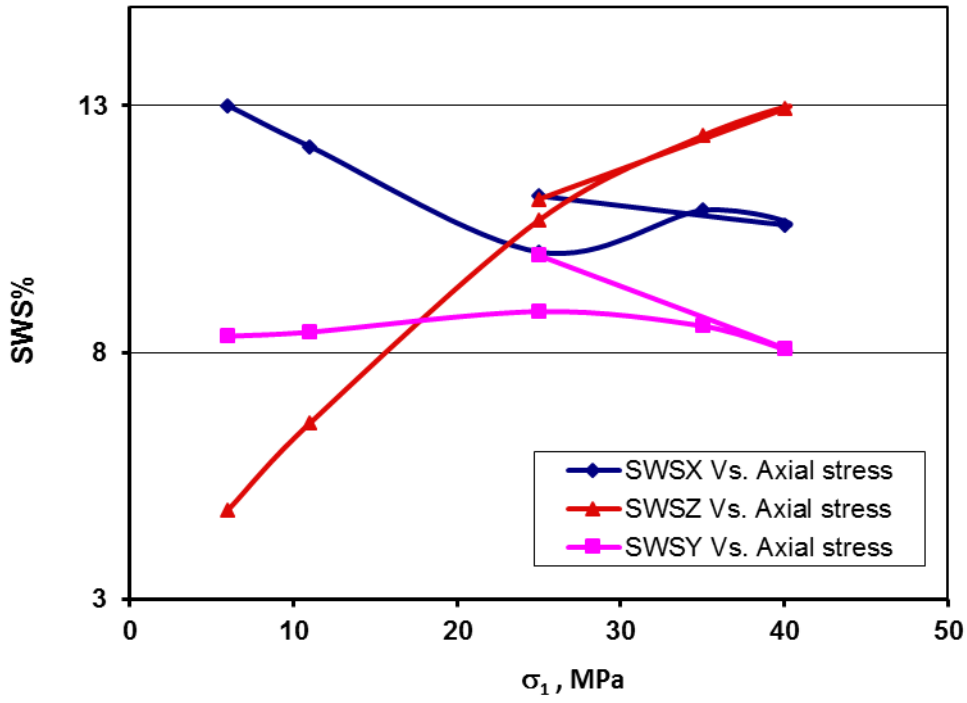

Figure 49. Variation of SWS as a function of axial stress for specimen TS-45^{o}-1.

4.3 Testing procedure for Tournemire shale specimens tested under a longer saturation period (four hours)

1. The specimen and the cell system, including all tubing, are flushed with de-aired water.
2. Bring the hydrostatic stress to 2 MPa and the back pressure to 1MPa gradually and simultaneously. This is maintained for four hours, and then the readings of confining pressure, back pressure, and pore pressure are taken.
3. With pore-pressure fluid drainage prevented, a 200 to 300 kPa increment of axial and confining pressure is applied.
4. The pore-pressure response is measured (i.e., record the pore-pressure increment), and the B-value is calculated as a ratio of the resulting increase in the pore pressure to the cell pressure increment.
5. The pressure in the back-pressure system is increased the same amount as the increment in the cell pressure (i.e., 200 kPa). The pore-pressure fluid drainage valves are opened to the back pressure to restore the initial effective stress.
6. With the new back-pressure level, steps 3, 4, and 5 are repeated. These incremental B-tests have been conducted for three pressure levels. The calculated B values were found to be, 0.3, 0.3, and 0.35 for the three steps of measurements described above.
7. The specimen is loaded hydrostatically up to 5 MPa while maintaining back pressure.
8. Follow steps 3 to 10 of the testing procedure described in section 3.1 to finish the test.

The pressures and the methodology based on which the B values were calculated for the specimen TS0°-2 are given in Figure 8 in Appendix A. Table 1 in Appendix A shows the initial moisture content of two Tournemire specimens.

4.3.1 Testing results for specimen TS0°-2

The TS0°-2 specimen has been tested based on the testing procedure explained above with special attention to measuring the B value after the specimen was under back water pressures for four hours. Figure 50 shows the variation of applied axial load, confining pressure, top pore water pressure and bottom pore water pressure as a function of time on the specimen for the

initial four hours of saturation period. Figure 51 shows variation of aforementioned parameters for the time period during which the B values were obtained. This specimen was failed at a 49 MPa axial stress.

The post failure residual strength was reduced to 32 MPa (Figure 52). Permeability values for four differential stresses have been determined during the test and one k value at post failure stress regime was measured. Figure 53 shows a specimen failure pattern characterized with fewer fractures running sub-parallel to the XZ plane of symmetry (in 3D sketch).

4.3.1.1 Evolution of ultrasonic wave velocities with differential stress increment, TS0^o-2

Figures 54 to 57 show the variation of the compressional (V_P), shear (Vs_1 and Vs_2) seismic wave velocities and shear wave splitting (SWS) as a function of axial stress for specimen TS0^o-2. The V_{PZ} continuously increases as a function of axial stress, which is parallel to the σ_1 direction up to a differential stress of 50 MPa. Similar to what has been observed in specimen TS0^o-1 (Figure 40), the V_{PZ} and V_{PX} show a higher value than V_{PY} due to the way the specimen was placed in the cell with respect to the 3D orientation of V_P sensors in the cell (Figure 52). The Y axis in the cell is oriented normally to the XZ plane of the specimen. Similar to specimen TS0^o-1 (Figure 41 and 42) the orientation of the specimen's pre-existing bedding plane is demonstrated to have a similar effect on shear wave velocities to that of the compressional wave velocity when evaluated with respect to the XZ plane. The two shear wave velocities propagated normally to each other (Figures 55 and 56) i.e., V_{S1Y} and V_{S2Y} are both much slower than the other two shear velocities measured along the Z and X axes.

Figure 57 shows SWS as a function of axial stress, measuring the anisotropic nature of Tournemire specimen TS0^o-2. The SWS for the X and Z axes shows a higher degree of anisotropy as a function of axial stress due to the presence of a XZ plane of symmetry.

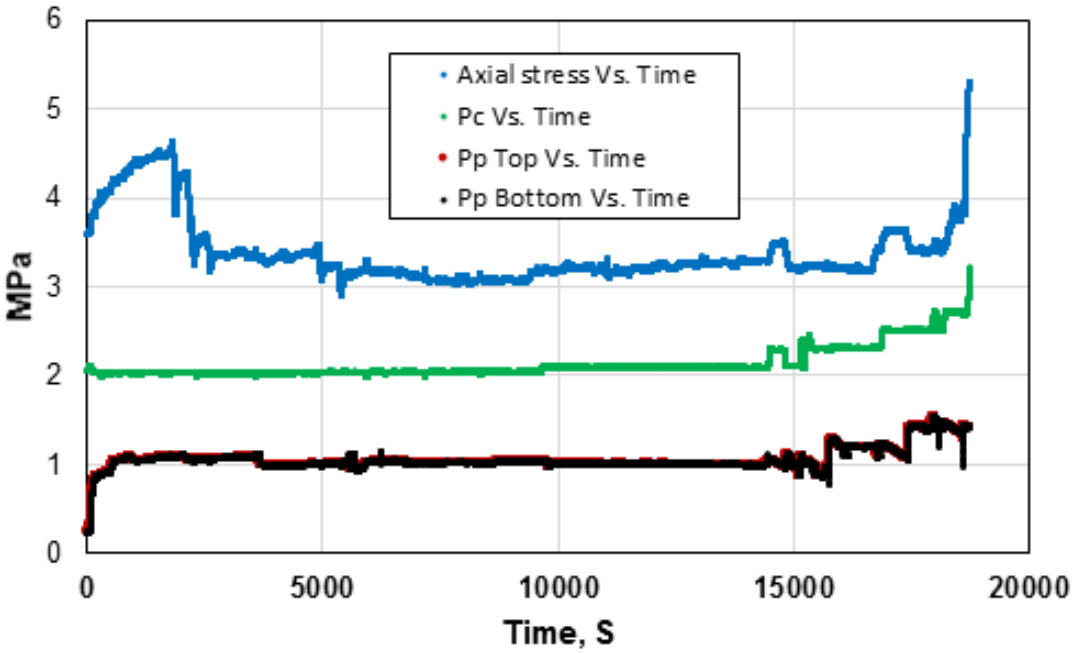

Figure 50. Variation of applied axial load (σ_1), confining pressure (P_C), top pore water pressure (P_P Top) and bottom pore water pressure (P_P Bottom) on the specimen for the initial four hours of in situ saturation period.

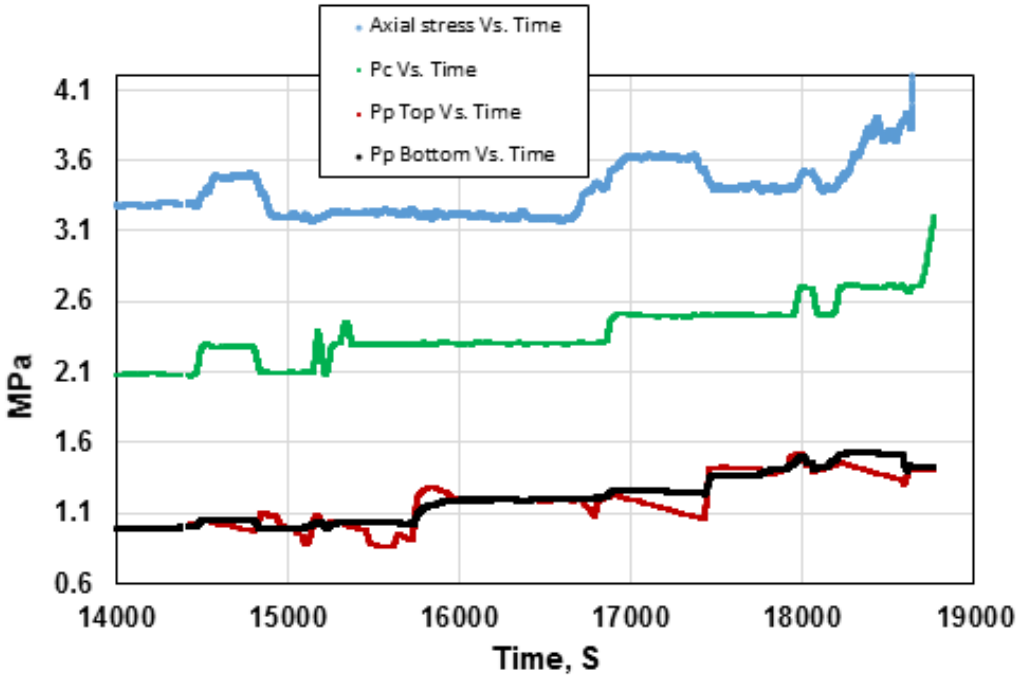

Figure 51. Variation of applied axial load, confining pressure, top pore water pressure, and bottom pore water pressure on the specimen during performing tests for calculating B values.

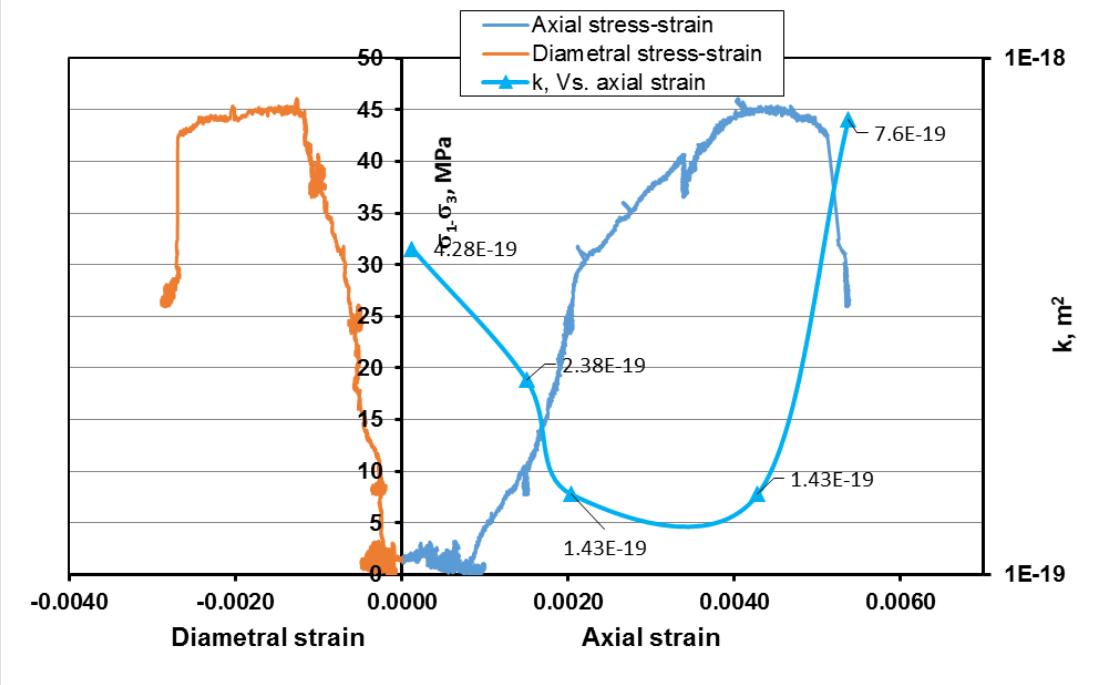

Figure 52. Variation of axial and diametral strains with differential stresses for specimen TS0^{o}-2 tested at 5 MPa confining and 3 MPa pore pressures, respectively. Variation of permeability as a function of axial strain is shown in the second vertical axis here.

Figure 53. Failure pattern (images in the middle) observed for the tested specimen TS0^{0}-2 with that of intact one (image on the left). The sketch shows the 3D orientation of wave velocity measurements with respect to the bedding planes.

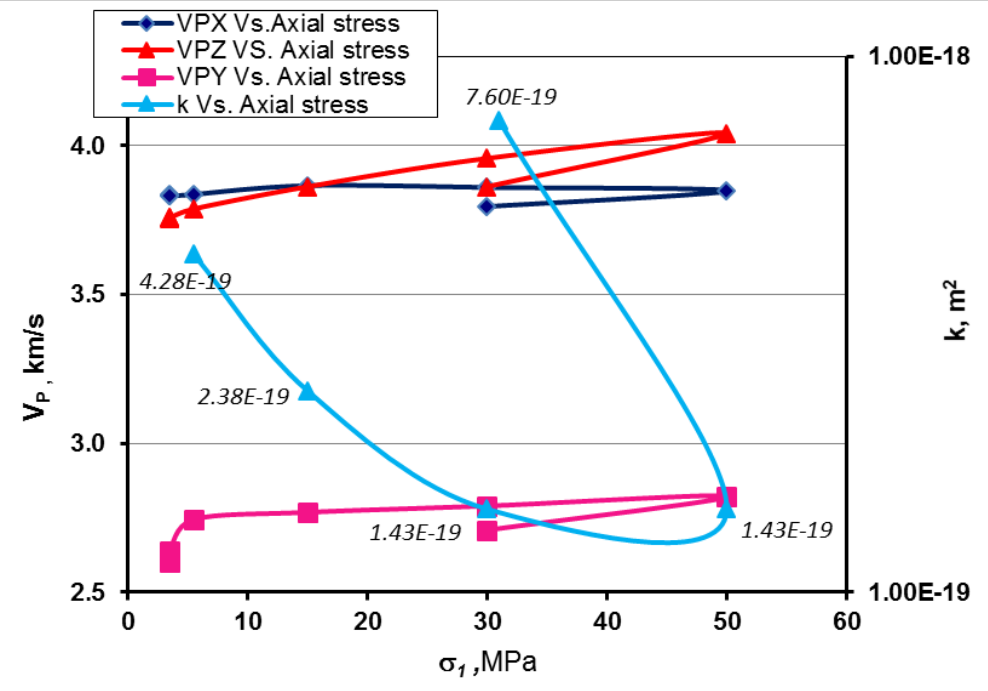

Figure 54. Variation of compressional wave velocities measured along the three orthogonal axes and permeability values with axial stress for the TS0°-2 specimen.

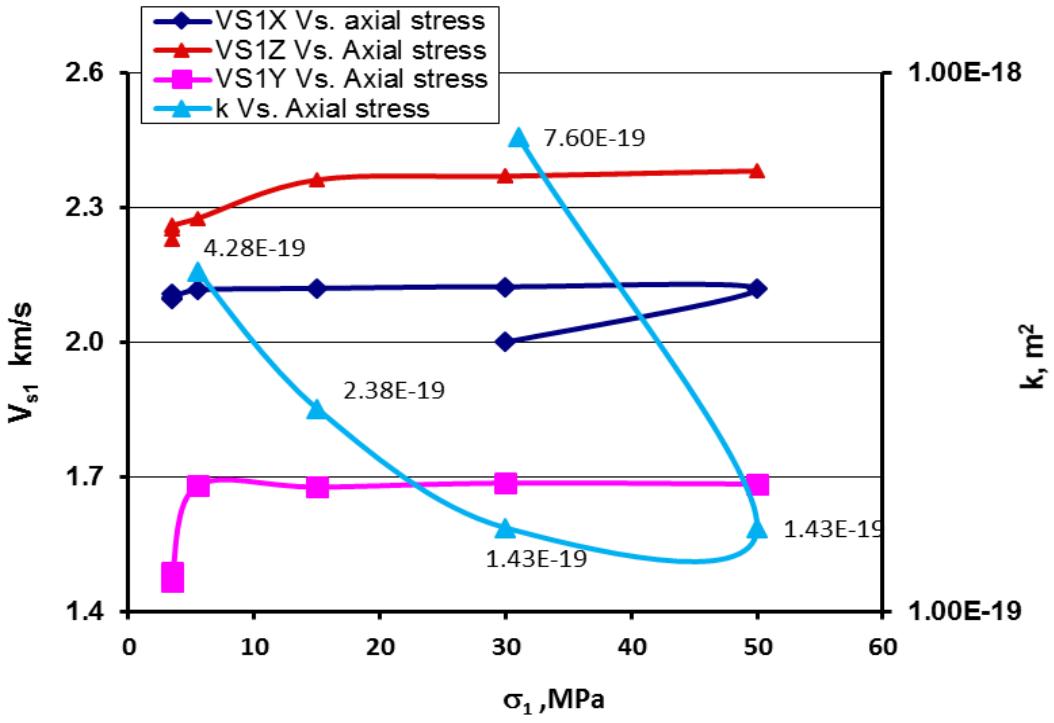

Figure 55. Variation of shear wave velocity V_{S1} and permeability as a function of axial stress.

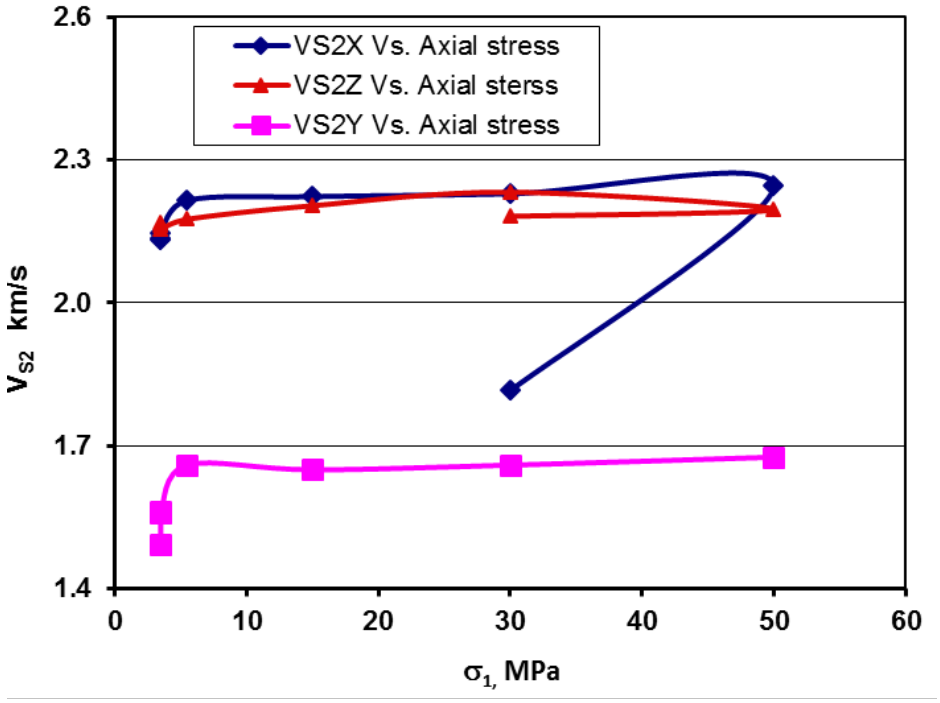

Figure 56. Variation of shear wave velocity V_{S2} as a function of axial stress.

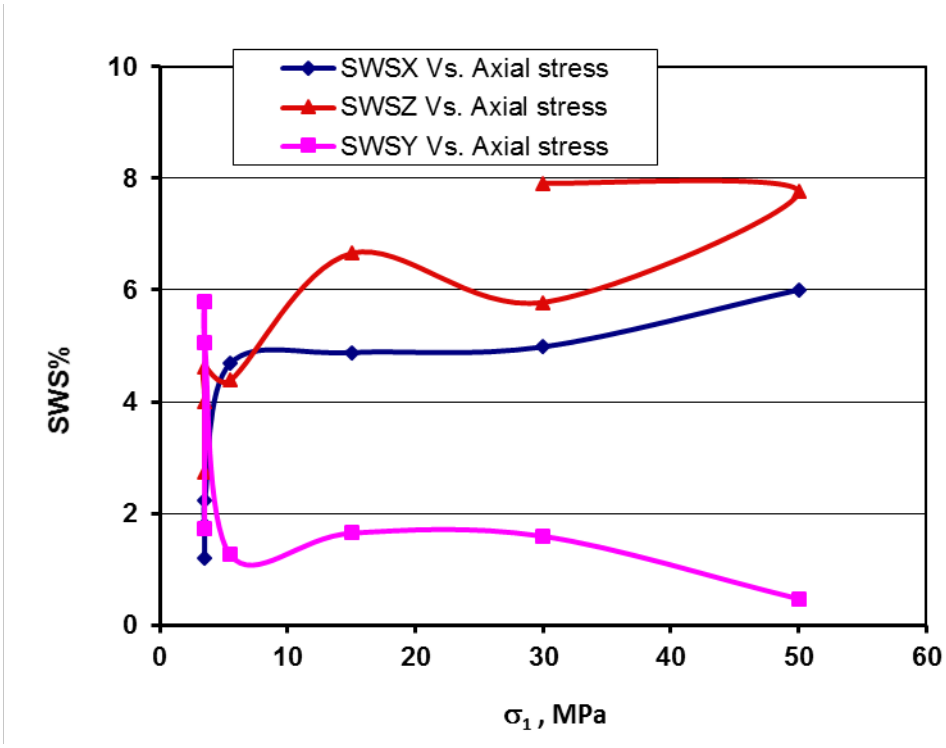

Figure 57. Variation of shear wave splitting SWS as a function of axial stress.

5 Summary and Conclusion

Table 3 summarizes the coupled hydro-mechanical properties of all tested specimens as a function of their foliation planes. The mechanical, hydraulic transport, and seismic properties of both rock types are influenced by the foliation plane orientation with respect to σ_1.

The test results obtained from hydro-mechanical experiments on three Cobourg limestone specimens prepared perpendicular to the foliation planes tested at 5 MPa of confining pressure show a failure strength of 56 MPa, 46 MPa, and 46 MPa, respectively, whereas the failure strength of the three specimens of Cobourg limestone tested parallel to the foliation planes show a failure strength of 90 MPa, 99 MPa, and 77 MPa, respectively. The latter three specimens show smaller axial deformations than the former three specimens. It is concluded that the specimens tested with their foliation planes oriented parallel to the σ_1 direction are stronger (55%) than the specimens tested with their foliation planes oriented perpendicular to the σ_1 direction, thereby confirming the anisotropic nature of this rock. Limited experiments performed on Tournemire shale indicate that this rock is anisotropic in nature as well. Specimens tested with the foliation plane oriented at 45^o with respect to σ_1 show a 12% strength reduction in comparison to specimens tested with their foliation planes oriented at 0^o with respect to σ_1.

Specimens of the Tournemire shale and Cobourg limestone tested at various angles with respect to their foliation planes show two different types of axial splitting and shearing type of failure patterns. This observation further confirms the fact that how differently oriented foliation planes interact with the main principal stress will lead to different types of failure patterns.

Figure 58 shows the variation of k as a function of axial stress for all six Cobourg limestone specimens. This comparative graph shows that the k value measured at the post peak stresses (representing the excavation damage zone hydraulic properties) can be 2 to 3 orders of magnitude higher than that of the intact rock irrespective to the foliation plane orientation.

Table 3. Hydro-mechanical properties of all tested rock specimens

Specimen	**σ_1 at failure** MPa	**Axial strain %**	**Diametral strain %**	**Max K** m^2	**Min K** m^2
Cobourg limestone					
CLH-3-T	90	0.45	0.54	8.9E-19	1.4E-19
CLH-1-U	99	0.45	0.18	3.9E-16	9.7E-20
CLH-3-U	77	0.46	0.30	1.5E-18	1.9E-19
CLV-3-T	50	0.30	0.30	1.8E-18	9.3E-20
CLV-1-U	56	0.65	0.32	8.8E-18	4.6E-20
CLV-5-T	46	1.50	-	1.0E-18	3.7E-19
Tournemire shale					
TS0^o-1	50	0.95	-	2.7E-19	4.2E-18
TS45^o	44	0.63	0.30	1.0E-19	5.0E-20
TS0^o-2	50	0.43	0.30	7.6E-19	1.4E-19

CLH represents specimens with their foliation planes oriented parallel to the σ_1 direction and CLV represents the specimens with their foliation planes oriented perpendicular to σ_1.

The curve showing the variation between the permeability as a function of axial stress for all six experiments on Cobourg limestone reported so far are characterized with similar features. The initial section of the curves is characterized with a higher value of k (measured with a very small differential stress). The second section of the curves is characterized with a decreasing trend of k when the specimens are undergoing a compressive regime and the third section of the curves shows an increase in k value at a much higher rate prior to peak strength associated with the formation of new micro-cracks aligned to the σ_1 direction. Variation of k as function of axial stress is confirmed by the evolution of wave velocity measurements as a function of axial stress and shows a similar trend.

Figure 59 shows the variation of k as a function of axial stress for all three specimens of Tournemire shale tested with their foliation planes oriented at 0^o and 45^o with respect to σ_1. It can be concluded that the specimen drilled at 45^o to the bedding planes is about one order of magnitude less permeable than the ones drilled at the 0^o orientation to the bedding planes. This can be due to more persistent and continuous nature of the parallel foliation planes in the Tournemire shale. The hydro-mechanical properties of the two rock types studied in this project are influenced by the degree and nature of their anisotropy at a different magnitude.

Figure 58. Variation of k as a function of axial stress for all six Cobourg limestone specimens.

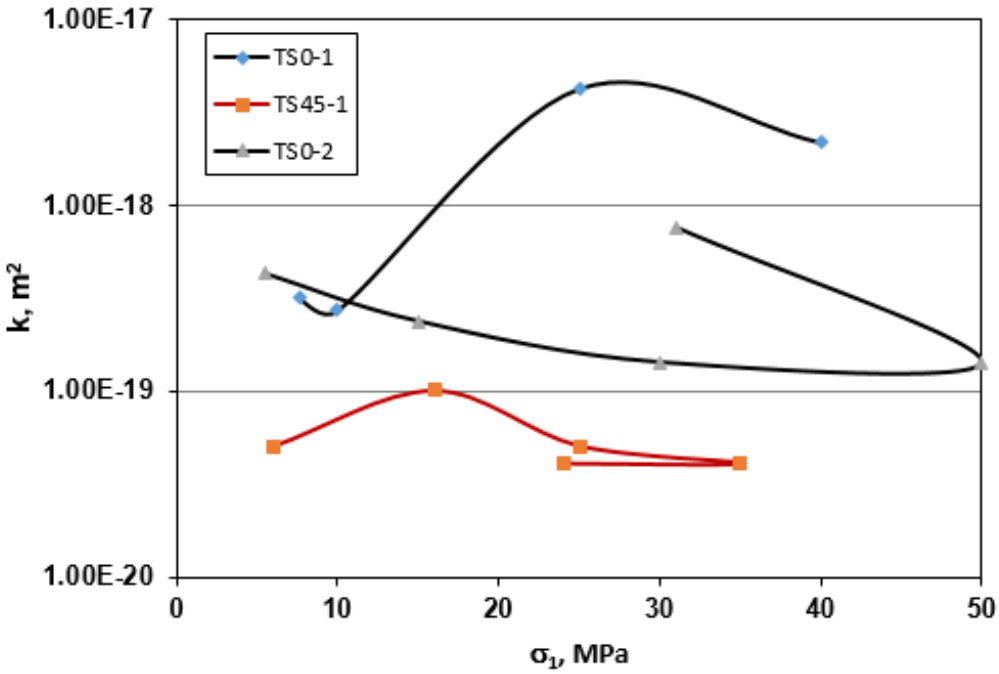

Figure 59. Variation of k as a function of axial stress for all three Tournemire shale specimens.

Variation of the degree of inherent anisotropy (maximum strength/minimum strength) from one rock type to another will affect the extent of the induced excavation damage zone differently. The extent of damage caused by excavation activities within anisotropic media is correlated with the degree and nature of anisotropy. Therefore, the assessment of degree of anisotropy, and its impact on the hydro-mechanical behaviour of the excavation damage zones and on the design and excavation of repositories and shafts become necessary.

Acknowledgements

We are grateful to the Canadian Nuclear Safety Commission for financial support of this research. Maria Tibbo, Mahdi Sehizadeh, and William Ye are sincerely acknowledged for their help in assisting with the specimen preparation.

References

Boulin PF, Bretonnier P, Glan N, and Lombard JM., 2012. Contribution of the steady state method to water permeability measurement in very low permeability porous media, Oil and Gas Science and Technology-Rev. IFP Energies nouvelles, Doi: 0.2516/ogst/2011169.

Brace WF, Walsh JB, and Frangos WT., 1968. Permeability of granite under high pressure. J Geophys Res, 73(6):2225–2236.

ISRM, 1981a, Part 1: Suggested method for determining water content, porosity, density, absorption and related properties. ISRM Suggested Methods; Rock Characterization testing and monitoring, Int. Soc. Rock Mech. Pp. 81-89.

Nasseri MHB, Goodfelow SD, Wanne TS, and Young RP., 2013. Coupled Thermo-Hydro-Mechanical properties of Cobourg limestone under hydrostatic and deviatoric stresses, IJRMMS, 61, 212–222.

Nasseri MHB, and Young RP, 2014. Thermo-Hydro-Mechanical properties of Cobourg limestone, Report number TR-2012-03 submitted to NWMO.

Roy DM, Scheetz BE, Pommersheim J, and Licasttro PH., 1993. Development of transient permeability theory and apparatus for measurements of cementitious materials, Material research laboratory, The Pennsylvania State University, University Park, Pennsylvania.

Selvadurai APS, and Jenner L., 2012. Radial flow permeability testing of an argillaceous limestone. Ground Water, Doi:10.111/j1745-6584.2012.00932.x.

Roy DM, Scheetz BE, Pommersheim J and Licasttro PH., 1993. Development of transient permeability theory and apparatus for measurements of cementitious materials, Material research laboratory, The Pennsylvania State University, University Park, Pennsylvania.

Appendix A

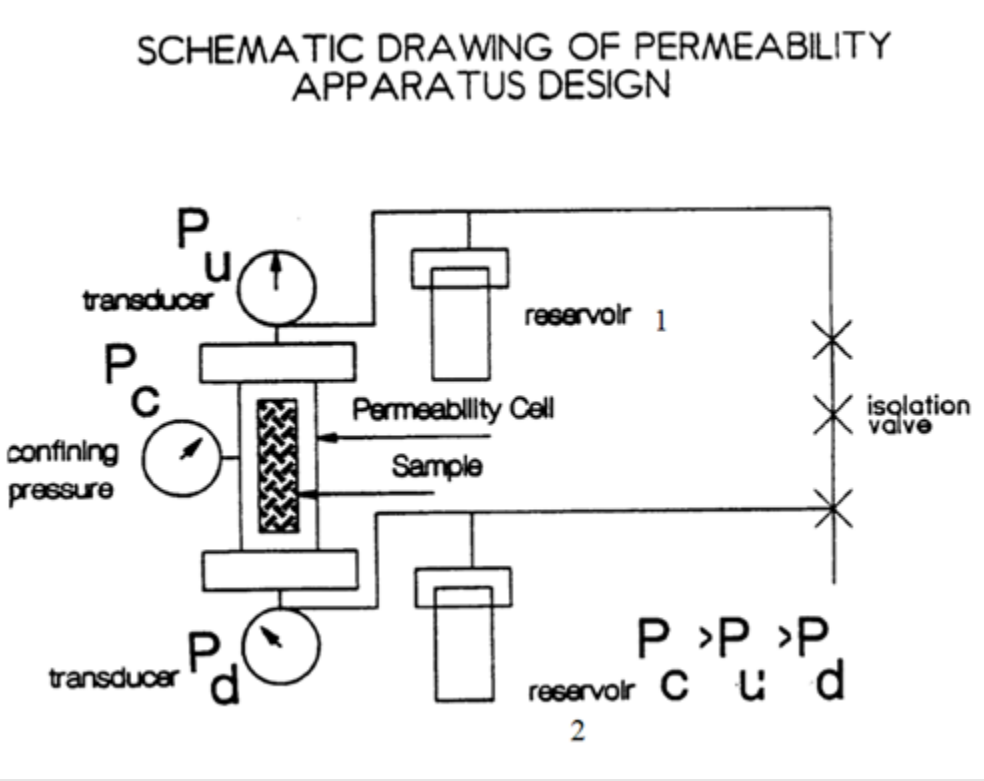

Figure 1. Schematic drawing of the permeability apparatus showing details of the pulse decay method. P_U = pore water pressure in the upstream side of the specimen, P_d = pore water pressure in the downstream side of the specimen, P_C = confining pressure, (Roy et al., 1993). During the test 1MPa hydraulic pulse was introduced from the top of the specimen.

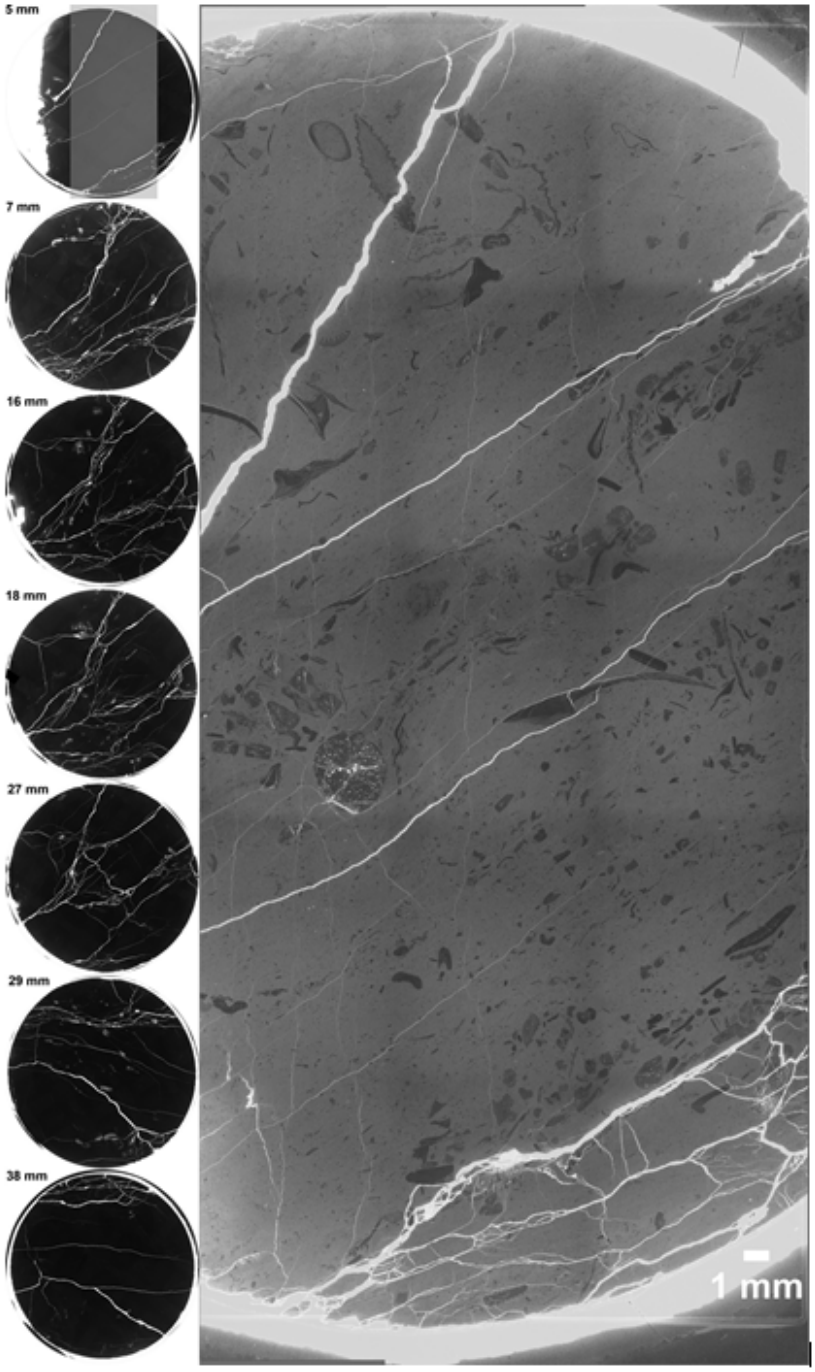

Figure 2. The macro-fracture distributions from top (7mm section) to the middle (38 mm cut) of the CLH-3-T Cobourg limestone specimen (50mm is the diameter of the black circles containing the macro-fractures) are shown on the left side of the figure. The thin section image shows the detail of micro-fracture distribution on the section prepared 7mm from the top of the specimen. 1mm long scale (coloured white) is shown at the bottom right of this thin section. Carbonaceous fossils are clearly shown embedded in the very fine clay matrix of Cobourg limestone, which was tested parallel to the foliation plane, and is shown in the image.

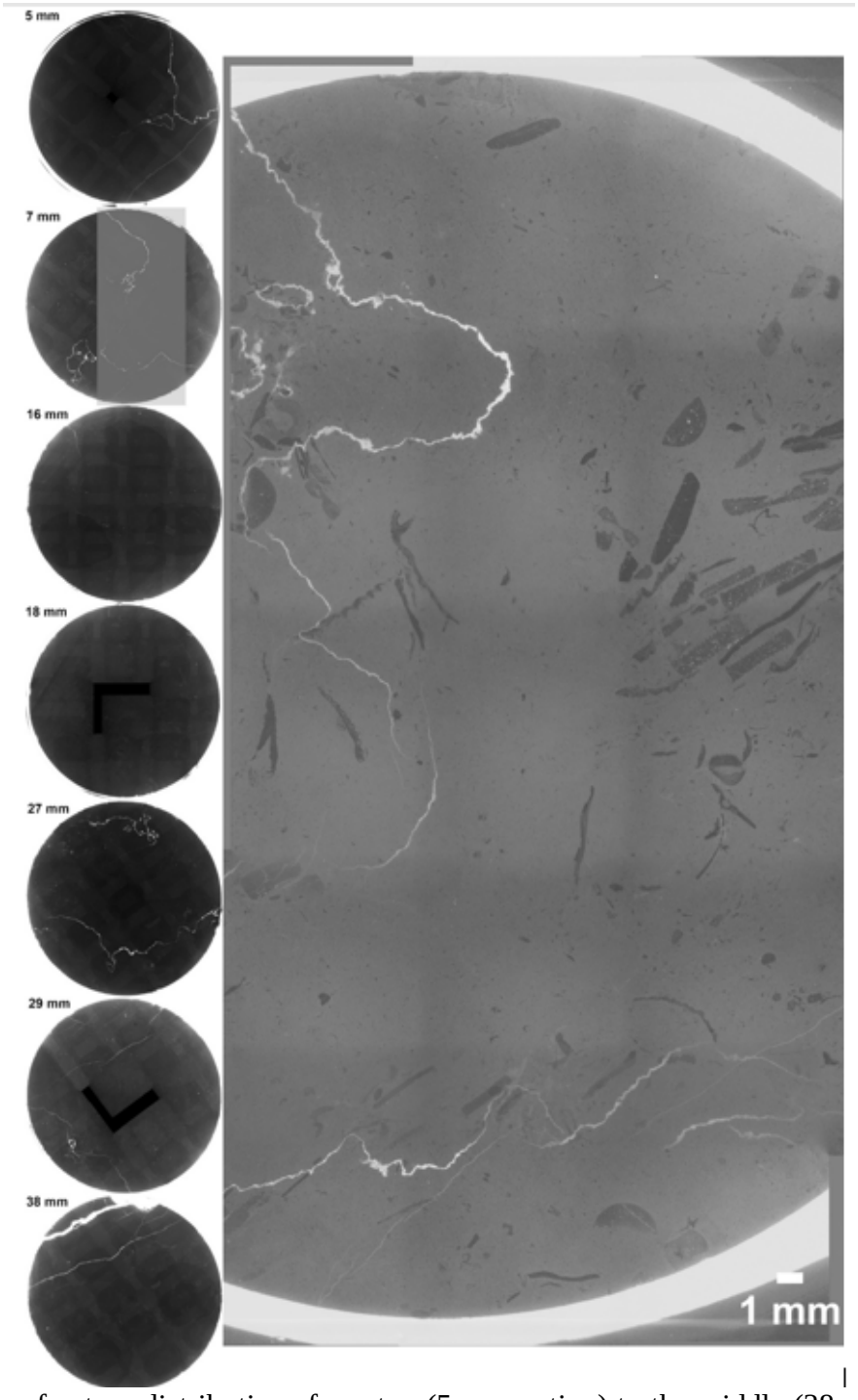

Figure 3. Macro-fracture distributions from top (5mm section) to the middle (38 mm section) of the CLV-3-T Cobourg limestone specimen are shown on the left side of the figure. The thin section image shows the detail of micro-fracture distribution on the section prepared 7mm from the top of the specimen. Carbonaceous fossils are clearly shown embedded in the very fine clay matrix of the Cobourg limestone, which was tested perpendicular to the foliation plane, and is shown in the image. The various sections and the thin section image are characterized with fewer fractures in comparison to the ones seen in figure 2.

Storage factor calculation for the pulse decay permeability measurment set-up using steel specimen

It is important to measure the storage factor of the testing set-up prior to pulse decay permeability measurements using a steel specimen within the testing set-up. Figure 4 shows such a set-up with a steel specimen in the cell, σ_1 was raised to 50 MPa axially and a confining pressure (P_C) was raised up to 30 MPa within the cell first. Next, using the quizix pump the pore water pressure was raised in steps up to 25 MPa (first by steps of 2 MPa up to 10 MPa and then by steps of 5 MPa up to 25 MPa) and the volume of water needed to pressurize each side of the steel sample was recorded. The presure was decreased the same way to plot the full cycles of the loading and unloading steps. The applied volume was checked to account for any possible leaks and thus the storage factor estimation was not affected (Figure 5). Figure 6 shows the comparison of the volume of water used to cause 25 MPa of water pressure during the loading and unloading stages. This variation indicates that the storage factor was not affected by any leakage issues. During this test, the delta Pp and the volume of water were recorded to calculate the storage factor. Figure 7 shows the variation of the calculated storage factor as a function of applied pore water pressure up to 20 MPa on the upstream side. The upstream storage factor decreased with pressure from 2.5E-10 m^2 to 1.3E-10 m^2, (Figure 7). The results obtained herein are consistent with the compressibilities obtained in the test procedure shown in Boulin et al. (2012).

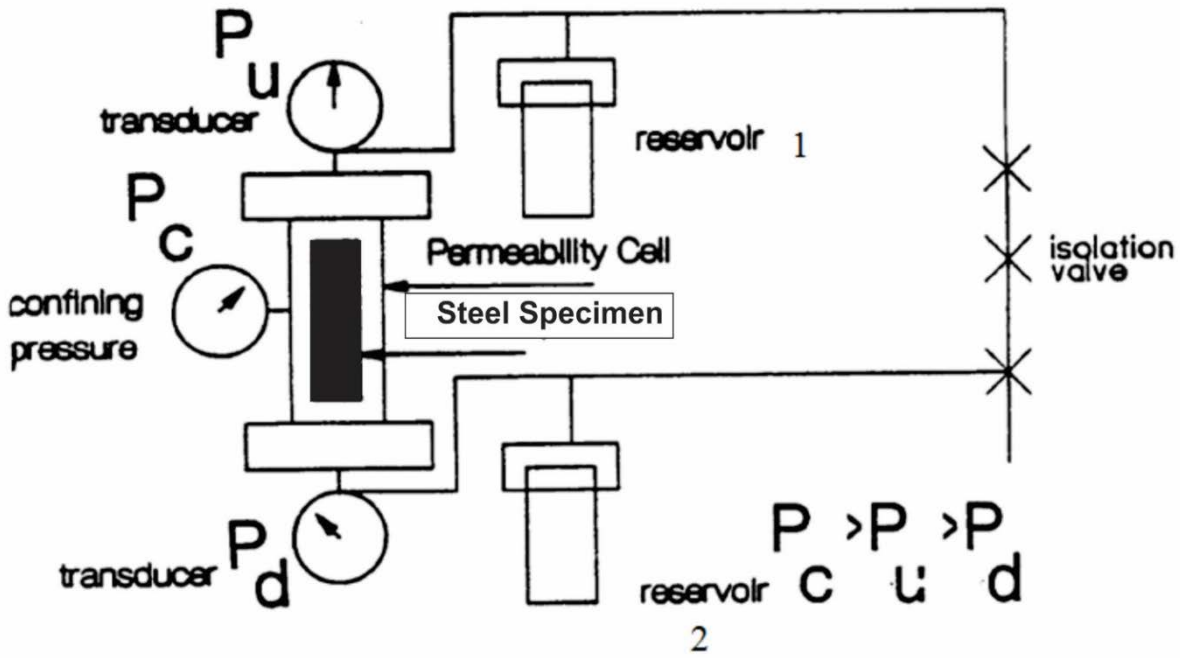

Figure 4. Modified schematic drawing of permeability apparatus showing details of pulse decay method with the steel specimen within the cell (Roy et al., 1993). The steel sample was used in our permeability testing set-up to measure reservoir storage values and its overall system compressibility. The results found in this calibration test are consistent with the compressibility shown in Boulin et al. (2012).

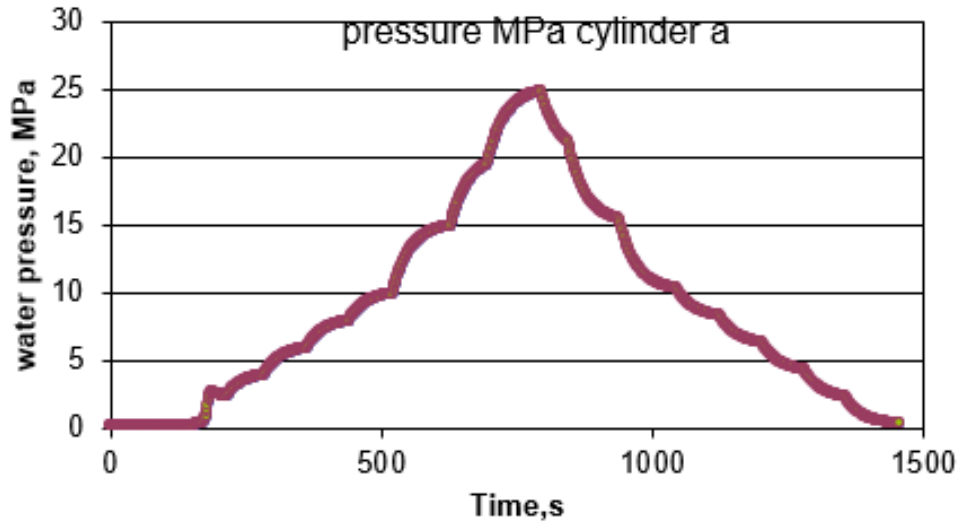

Figure 5. Variation of applied pore water pressure (Pp) as a function of time tested on the top platen (reservoir 1) within the peremeability test set-up.

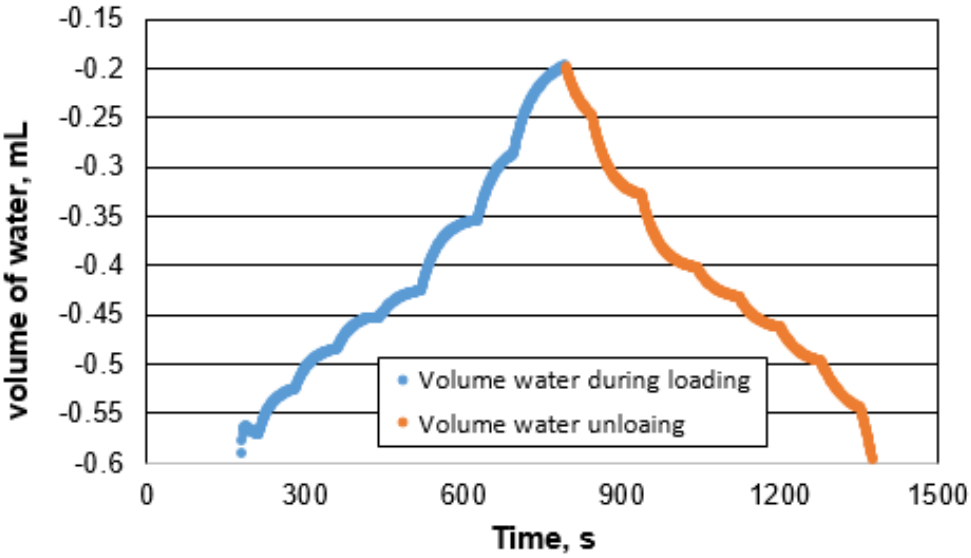

Figure 6. Variation of volume of water used during pore water pressure loading and unloading steps up to 25 MPa within the cell with steel specimen.

Following equation (1) is used to calculate the storage factor for upstream side of testing set-up:

$$S(u) = \rho w * g * Vu,d/dPw \quad (1)$$

Where, *S(u)* storage factor of upstream reservoir, ρ_w = water density, *g* = gravity, *Vu,*= volume of water to pressurize upstream reservoir and *dPw* = delta water pressure. Figure 6 shows the variation of storage factor as a function of applied water pressure for the testing set-up.

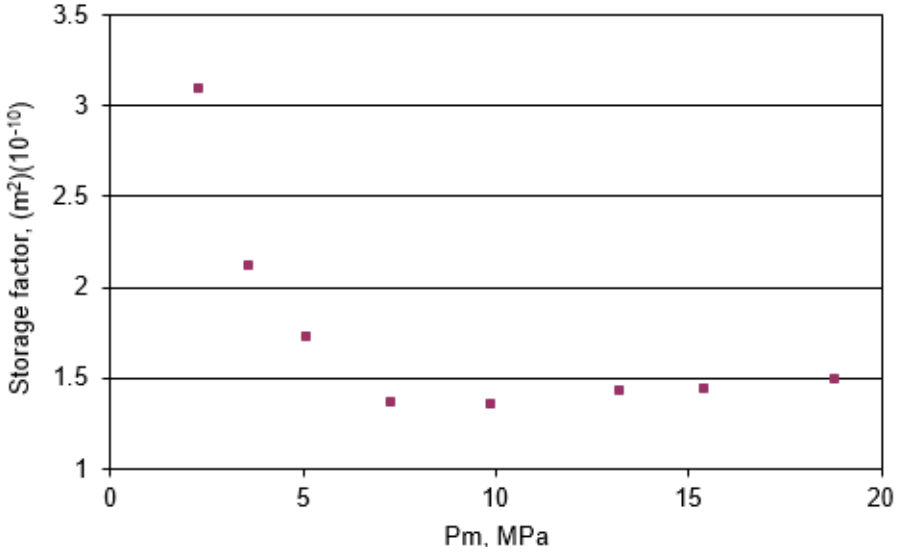

Figure 7. Variation of storage factor as a function of applied pore water pressure for the upstream reservoir.

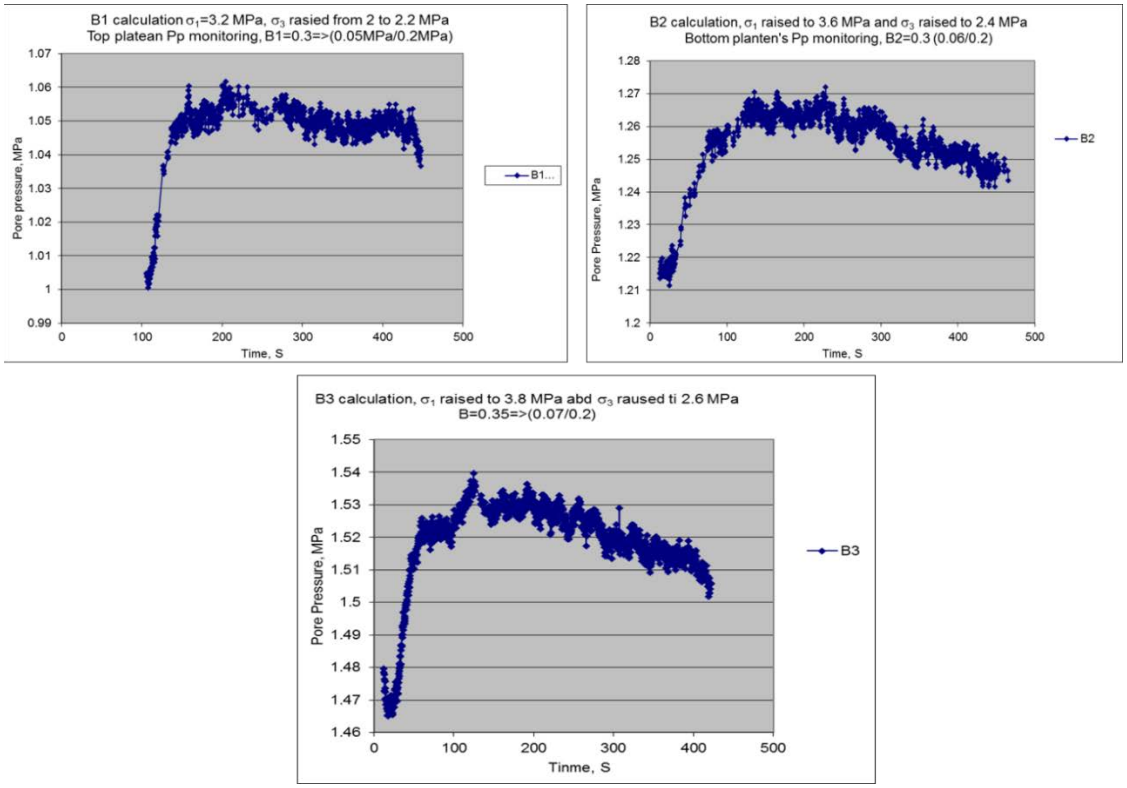

Figure 8. Pore water pressure responses as a function of time for the three stress levels at which B values were evaluated for specimen TS0^o-2.

Table 1. Moisture content of two Tournemire shale specimens.

Sample Name	Length mm	Diameter mm	Initial Room Temp. Weight gr	Final Dry Weight, gr	Moisture Content, %
M-21-9	123.90	49.35	593.66	581.47	2.05
M-21	142.91	37.81	403.77	395.31	2.09

*Final dry weight was achieved after getting a constant dry weight within a period of two months of drying process.